On Particle Shifting Techniques (PSTs): Analysis of existing laws and proposition of a convergent and multi-invariant law

J. Michel, A. Vergnaud, G. Oger, C. Hermange, D. Le Touzé

Available online at www.sciencedirect.com
ScienceDirect
Journal of Computational Physics 00 (2022) 1–40
Journal of Computational Physics

On Particle Shifting Techniques (PSTs): analysis of existing laws and proposition of a convergent and multi-invariant law

J. Michel[a,b], A. Vergnaud[a], G. Oger[a], C. Hermange[b], D. Le Touzé[a]

[a] *Ecole Centrale Nantes, LHEEA research dept. (ECN and CNRS), Nantes, France*
[b] *La Manufacture Française des Pneumatiques Michelin, Clermont-Ferrand, France*

Abstract

This paper addresses the Particle Shifting Technique (PST) in the SPH schemes. Improving the accuracy of SPH schemes leads to particle clustering along the flow streamlines which turns to be detrimental for the simulations. PSTs aim at avoiding this adverse effect by slightly disordering the particles, allowing to retrieve a regular particle distribution within the kernel interpolation support. The gain in accuracy is such that this technique is now commonly adopted by the SPH practitioners, however the conditions that should be respected by a PST are not clearly discussed in the literature. In this paper, such conditions are exposed and their fulfillment by the main existing PSTs of the literature is analyzed. None of these existing PSTs fully satisfying these conditions, a novel PST is introduced. The proposed PST is validated for three different SPH schemes on 2D and 3D test cases, in presence of free-surface and solid boundaries.

Keywords: Smoothed Particle Hydrodynamics; Particle Shifting Technique

1. Introduction

The Smoothed Particle Hydrodynamics (SPH) method suffers from the presence of anisotropic particle structures inherent to its Lagrangian feature [22, 39, 17, 25]. While this effect appears when improving the scheme accuracy, it tends paradoxically to degrade the kernel interpolation due to the irregular particle distribution obtained within the compact support. The Particle Shifting Technique (PST) sounds as a suitable tool to remedy this problem as it is increasingly discussed in the SPH literature [22, 37, 39, 17, 31, 25, 11, 33, 32]. The principle of the PST is to move slightly the particles from their Lagrangian trajectories in order to recover a regular particle distribution in space. This is achieved by adding a small perturbation $\boldsymbol{\delta u}$ within the velocity field [22, 25, 32] or by introducing a modification $\boldsymbol{\delta r}$ in the particle positions [39, 17, 11, 33].

The first PST was introduced by Monaghan [22] in the compressible SPH context in order to avoid particle clustering. The PST velocity $\boldsymbol{\delta u}$ introduced in that paper was Galilean invariant and was applied to update particle positions exclusively, i.e. without being taken into account in the continuity and momentum equations. In [17], a new PST was introduced within the projection-based Incompressible SPH (ISPH) formalism, compatible with the presence of a free-surface. It was achieved by using a PST displacement $\boldsymbol{\delta r}$ based on Fick's law, providing a shifting of the particles from areas of high concentration to those of

*Corresponding author
Email address: julien.michel@ec-nantes.fr (J. Michel)

low concentration. Since the introduction of a PST based on Fick's law, various adaptations have been performed for different SPH schemes: (i) using Arbitrary Lagrangian Eulerian (ALE) formalism by Oger *et al.* [25], (ii) using δ-stabilization term by Sun *et al.* [33, 32], (iii) in the ISPH context by Khayyer *et al.* [11], (iv) in another context to initialize correctly an SPH simulation using the particle packing algorithm derived by Colagrossi *et al.* [8]. Although these PSTs have been validated through various challenging test cases, the conditions that should be respected by a PST have not been addressed clearly in the SPH literature.

This paper aims at proposing a list of conditions that any PST should verify from our point of view, and then to introduce a methodology to build it. To this end, a theoretical study of already existing PSTs is carried out in one dimension, derived from the results obtained by Quinlan *et al.* [27] about the truncation error of SPH operators. Thereafter, a methodology that fulfills these conditions is introduced together with a novel PST law satisfying them. The theoretical results are obtained in one dimension. Therefore, verifying them numerically in two and three dimensions is crucial, as outlined in Sections 4, 5, 6 and 7.

Specifically, Section 4 addresses this verification without free-surface or solid boundary, and the validation of the proposed PST is performed for three Weakly-Compressible SPH schemes briefly reminded in Section 4.2. In Section 5, the theoretical results of Quinlan *et al.* [27] are extended close to a free-surface for the needs of the present paper. The extension of the proposed PST in presence of a free-surface is then presented and validation is performed. In Section 6, the theoretical results are verified in presence of both a free-surface and a solid boundary using the moving ghost particle method to model the solid boundaries. Finally in Section 7 the validation is performed using a boundary-integral method to model the solid boundaries.

2. PST in the SPH literature

2.1. Monaghan [22]

The first PST was proposed by Monaghan [22] in order to avoid particle clustering. It reads:

$$\boldsymbol{\delta u}_i^{MON} = 2\epsilon \sum_{j\in\mathcal{D}_i} V_j\rho_j \left(\frac{\boldsymbol{u}_j - \boldsymbol{u}_i}{\rho_i + \rho_j}\right) W_{ij} \ , \tag{1}$$

where ϵ is a parameter, typically set to $\epsilon = 0.5$. $\boldsymbol{\delta u}$, $\boldsymbol{u}$, ρ and V stand for the PST velocity, the Lagrangian velocity, the density and the volume associated the particles, respectively, while W is the kernel and $\mathcal{D}_i$ the kernel support. This PST has the advantage of being Galilean invariant. In [22], $\boldsymbol{\delta u}_i^{MON}$ was used to update the particle position exclusively, i.e. without any modification of the continuity and momentum equations, leading to the so-called XSPH method.

Note that by construction of $\boldsymbol{\delta u}_i^{MON}$ and its use to update the particle position exclusively, the following properties are ensured with the XSPH method: (i) the center of mass moves equivalently with or without this added PST velocity, (ii) the linear and angular momentum are conserved. Despite these properties, there is no clear reason for which $\boldsymbol{\delta u}_i^{MON}$ could point towards zones of low concentration of particles, as it is not derived from Fick's law.

2.2. Lind et al. [17]

In [17], a PST based on Fick's law was introduced, using the gradient of the particle concentration $\boldsymbol{\nabla} C_i$. $\boldsymbol{\nabla} C_i$ was computed through the approximation of $\boldsymbol{\nabla} 1$ as defined in Eq. (2) (i.e. with $C \equiv 1$) corresponding to a vector pointing towards the zone of high concentration of particles [8]. Therefore, $-\boldsymbol{\nabla} C_i$ is a vector pointing towards zones of low concentration of particles and sounds as a relevant basis of a PST.

$$\boldsymbol{\nabla} C_i = \sum_{j\in\mathcal{D}_i} \boldsymbol{\nabla}_i W_{ij} V_j \ . \tag{2}$$

Nevertheless, the following modified expression firstly derived by Monaghan [23] to prevent tensile instability was preferred in [17]:

$$\widehat{\boldsymbol{\nabla}} C_i = \sum_{j \in \mathcal{D}_i} \left[1 + 0.2 \left(\frac{W_{ij}}{W(\Delta x_i)} \right)^4 \right] \boldsymbol{\nabla}_i W_{ij} V_j \ , \tag{3}$$

where Δx_i is the characteristic distance between two adjacent particles. To obtain a displacement, the concentration gradient approximation $\widehat{\boldsymbol{\nabla}} C_i$ was then multiplied by $0.5h^2$, with h the smoothing length of the kernel support. However, using $\boldsymbol{\delta r}_i = -0.5h^2 \widehat{\boldsymbol{\nabla}} C_i$ as it is may lead to a PST displacement higher than the smoothing length. To prevent such strong PST displacements, an upper limit of $0.2h$ was imposed leading finally to:

$$\boldsymbol{\delta r}_i^{LEA} = \begin{cases} -0.5h^2 \widehat{\boldsymbol{\nabla}} C_i & \text{if } \left\| 0.5h^2 \widehat{\boldsymbol{\nabla}} C_i \right\| < 0.2h \\ -0.2h \dfrac{\widehat{\boldsymbol{\nabla}} C_i}{\left\| \widehat{\boldsymbol{\nabla}} C_i \right\|} & \text{otherwise} \end{cases} . \tag{4}$$

The PST displacement defined in Eq. (4) was also used by Khayyer *et al.* [11] with the difference that $\boldsymbol{\nabla} C_i$ was used instead of $\widehat{\boldsymbol{\nabla}} C_i$.

Although the PST was presented in terms of displacement in [17], note that it can also be rewritten as a velocity term using a time derivation approximation, as:

$$\boldsymbol{\delta u}_i^{LEA} = \begin{cases} -0.5h \dfrac{h}{\Delta t} \widehat{\boldsymbol{\nabla}} C_i & \text{if } \left\| 0.5h \dfrac{h}{\Delta t} \widehat{\boldsymbol{\nabla}} C_i \right\| < 0.2 \dfrac{h}{\Delta t} \\ -0.2 \dfrac{h}{\Delta t} \dfrac{\widehat{\boldsymbol{\nabla}} C_i}{\left\| \widehat{\boldsymbol{\nabla}} C_i \right\|} & \text{otherwise} \end{cases} , \tag{5}$$

where Δt denotes the time step.

2.3. Oger et al. [25]

The ALE formalism originally derived by Vila [37] was studied by Oger *et al.* [25] in the Weakly-Compressible SPH context. Using such an ALE formalism, a PST written in terms of velocity was required because the transport velocity (and consequently the PST velocity) appears explicitly in the SPH equations. The authors chose the approximation defined in Eq. (2). Multiplying $\boldsymbol{\nabla} C_i$ by a characteristic length d^{char} was required to obtain a non-dimensional vector. The authors chose $d^{char} = R$ where R is the kernel support radius. Then a characteristic velocity U^{char} had to be used and the authors chose $U^{char} = Ma\ c_0$, with Ma the Mach number and c_0 the nominal speed of sound (both taken as constant in time and space and defined prior to the simulation). Similarly to Lind *et al.* [17], the PST velocity was limited using a percentage of the Lagrangian velocity of the particles. This PST velocity finally reads:

$$\boldsymbol{\delta u}_i^{OEA} = \begin{cases} -Ma\ c_0 R \boldsymbol{\nabla} C_i & \text{if } \| Ma\ c_0 R \boldsymbol{\nabla} C_i \| < 0.25 \| \boldsymbol{u}_i \| \\ -0.25 \| \boldsymbol{u}_i \| \dfrac{\boldsymbol{\nabla} C_i}{\| \boldsymbol{\nabla} C_i \|} & \text{otherwise} \end{cases} . \tag{6}$$

2.4. Sun et al. [32]

Using the δ stabilization terms, Sun *et al.* [32] proposed another PST written in terms of velocity. The characteristic length $d^{char} = 2h$ was used, and similarly to Oger *et al.* the characteristic velocity was taken as $U^{char} = Ma\ c_0$. The main difference with respect to Eq. (6) resides in the use of $\widehat{\boldsymbol{\nabla}} C_i$ instead of $\boldsymbol{\nabla} C_i$. Furthermore, the limitation was not based on the Lagrangian particle velocity itself but on using the expected maximum Lagrangian velocity U_{max} throughout the fluid domain. Finally, the PST reads:

$$\boldsymbol{\delta u}_i^{SEA} = \begin{cases} -Ma\ c_0 (2h) \widehat{\boldsymbol{\nabla}} C_i & \text{if } \left\| Ma\ c_0 (2h) \widehat{\boldsymbol{\nabla}} C_i \right\| < 0.5 U_{max} \\ -0.5 U_{max} \dfrac{\widehat{\boldsymbol{\nabla}} C_i}{\left\| \widehat{\boldsymbol{\nabla}} C_i \right\|} & \text{otherwise} \end{cases} . \tag{7}$$

2.5. Summary of existing PSTs based on Fick's law

As a summary, different PST velocities using Fick's law can be designed using the following ideas: (i) use a vector pointing towards the zone of low concentration of particles $\tilde{\boldsymbol{\nabla}}C_i$, (ii) choose a characteristic length d^{char} linked to the kernel support, (iii) choose a characteristic velocity U^{char}, (iv) limit the PST velocity amplitude to a certain value U^{lim}. Then, these PST velocities can be written using the following generic formulation:

$$\boldsymbol{\delta u}_i^{gen} = \begin{cases} U^{char} d^{char} \tilde{\boldsymbol{\nabla}} C_i & \text{if } \left\| U^{char} d^{char} \tilde{\boldsymbol{\nabla}} C_i \right\| < U^{lim} \ , \\ U^{lim} \dfrac{\tilde{\boldsymbol{\nabla}} C_i}{\left\| \tilde{\boldsymbol{\nabla}} C_i \right\|} & \text{otherwise} \ , \end{cases} \tag{8}$$

with the parameters listed in Tab. 1.

	Characteristic length d^{char}	Characteristic velocity U^{char}	Pointing vector $\tilde{\boldsymbol{\nabla}}C_i$	Limitation U^{lim}
Lind *et al.* [17]	h	$\dfrac{h}{\Delta t}$	$-\widehat{\tilde{\boldsymbol{\nabla}}}C_i$	$0.2\dfrac{h}{\Delta t}$
Oger *et al.* [25]	R	$Ma\ c_0$	$-\boldsymbol{\nabla}C_i$	$0.25\left\|\boldsymbol{u}_i\right\|$
Sun *et al.* [32]	$2h$	$Ma\ c_0$	$-\widehat{\tilde{\boldsymbol{\nabla}}}C_i$	$0.5\ U_{max}$

Table 1: Summary of the existing PSTs based on Fick's law.

Then, for the PST velocities in Table 1, d^{char} is constant for all the particles during the simulation (without refinement technique), i.e. it is constant in space and time. Because of the fixed relation between h and R once the kernel chosen, throughout the rest of the paper R will be used instead of d^{char} for readability purposes, but the theoretical results obtained in this paper are valid using $d^{char} = h$ and $d^{char} = R$.

U^{char} is also constant in space and time in Oger *et al.* [25] and Sun *et al.* [32] since Ma and c_0 are constant. It is also the case for the PST velocity derived from Lind *et al.* [17] with the weakly-compressible assumption, as the time step computation is based on c_0. In contrast, U^{char} varies in time with the incompressible assumption since the CFL condition is based on the maximum Lagrangian velocity appearing within the fluid flow. However, it remains constant in space at any instant.

The limitation velocity U^{lim} is also constant in space and time in [32], contrary to [25]. For the PST velocity derived from [17], U^{lim} behaves similarly to U^{char}.

Furthermore, it is important to note that the PST velocities of Oger *et al.* and Sun *et al.* are not compatible with the incompressible assumption (presence of c_0), and that the PST velocity derived from Lind *et al.* is expressed differently considering the incompressible or the weakly-compressible assumption, as above-mentioned.

3. Expected requirements of a PST

This section addresses the conditions that should be fulfilled by a PST from our point of view. The first condition is to enforce the PST velocity to tend towards zero while refining the spatial resolution, which stands as a consistency requirement. The second condition is the Galilean invariance of the PST as proposed initially in [22] with the additional local rotation invariance. The third condition is the independence between local PST and global behavior of the fluid flow solution.

3.1. Consistency of the PST velocity

Unlike other numerical methods such as the Finite Volume method for instance, in the SPH method two convergence criteria are requested: $\Delta x \to 0$ and $\dfrac{\Delta x}{R} \to 0$. Practically, the second criterion is impossible to fulfill as a finite number of neighbor particles is expected within the kernel support. Therefore, SPH simulations are usually performed using a constant $R/\Delta x$ ratio. Thus, as far as the PST is concerned, the first condition that should be imposed is:

$$\lim_{\substack{\Delta x \to 0 \\ \frac{R}{\Delta x} = cst}} \boldsymbol{\delta u}_i = \mathbf{0} \ . \tag{9}$$

This condition is particularly important for an SPH scheme in which the PST is used to update particle positions exclusively, i.e. without being taken into account in the continuity and momentum equations, like in [22] and [33] for example. Note that this requirement can be theoretically alleviated when using an ALE formalism, since spatial differential operators are included in the continuity and momentum equations to take into account the additional terms due to the presence of a PST velocity [37, 25, 7]. Nevertheless, in practice the mass and volume of isolated particles can strongly deviate from their initial values, which causes some adverse consequences on the solution [7, 21]. Thus, condition (9) is suitable for these two families of SPH schemes.

In order to establish the convergence property of a PST velocity written using the generic formulation (8), we start here by studying $\boldsymbol{\nabla} C_i$. From Quinlan *et al.* [27], the truncation error of the gradient of a function A can be estimated in one dimension using Eq. (10), where ξ is a measure of the disorder within the particle distribution.

$$\begin{aligned}\sum_{j\in\mathcal{D}_i} A_j \boldsymbol{\nabla}_i W_{ij} V_j - A'_i = \frac{A_i}{R}\left[\xi O\left(\left(\frac{\Delta x}{R}\right)^3\right) + \frac{1}{2}\left(\xi^2 + \frac{1}{12}\right) O\left(\left(\frac{\Delta x}{R}\right)^4\right)\right] \\ + A'_i\left[\xi O\left(\left(\frac{\Delta x}{R}\right)^3\right) + O\left(\left(\frac{\Delta x}{R}\right)^4\right)\right] \\ + A''_i R\left[\xi O\left(\frac{\Delta x}{R}\right) + O\left(\left(\frac{\Delta x}{R}\right)^4\right)\right] + \dots \ .\end{aligned} \tag{10}$$

In our case, we are interested in $A \equiv 1$, leading to:

$$\boldsymbol{\nabla} C_i = \sum_{j\in\mathcal{D}_i} \boldsymbol{\nabla}_i W_{ij} V_j = \frac{1}{R}\left[\xi O\left(\left(\frac{\Delta x}{R}\right)^3\right) + \frac{1}{2}\left(\xi^2 + \frac{1}{12}\right) O\left(\left(\frac{\Delta x}{R}\right)^4\right)\right] \ . \tag{11}$$

Then, multiplying $\boldsymbol{\nabla} C_i$ by the characteristic length R leads to the following property:

$$R\boldsymbol{\nabla} C_i = O\left(1\right) \ , \tag{12}$$

when considering a fixed ratio $R/\Delta x$.

Therefore, since the velocities U^{char} and U^{lim} introduced in Tab. 1 are $O\left(1\right)$, the following conclusions can be drawn for all the PSTs introduced in Tab. 1:

1. In terms of velocity, $\boldsymbol{\delta u}_i = O\left(1\right)$ and then:

$$\lim_{\substack{\Delta x \to 0 \\ \frac{R}{\Delta x} = cst}} \boldsymbol{\delta u}_i \neq \mathbf{0} \ . \tag{13}$$

2. In terms of displacement, $\boldsymbol{\delta r}_i = O(\Delta x)$ and then:

$$\lim_{\substack{\Delta x \to 0 \\ \frac{R}{\Delta x} = cst}} \boldsymbol{\delta r}_i = \mathbf{0} \ . \tag{14}$$

This property is highlighted numerically in [32].

As a consequence, in order to recover the consistency condition (9) for a PST velocity written in the generic form (8), a relevant choice is to consider a characteristic velocity such that:

$$\lim_{\substack{\Delta x \to 0 \\ \frac{R}{\Delta x} = cst}} U^{char} = 0 \ . \tag{15}$$

We can observe that there is theoretically no need for a specific condition regarding U^{lim}, provided that the property (15) is satisfied. Conversely, if the condition (15) is not fulfilled, another way to comply with the condition (9) is to ensure that:

$$\lim_{\substack{\Delta x \to 0 \\ \frac{R}{\Delta x} = cst}} U^{lim} = 0 \ . \tag{16}$$

It can be observed that for the consistency property of the PST velocity, there is no restriction on U^{char} and U^{lim} of being local or global in space and time.

Note that using $\widehat{\boldsymbol{\nabla}} C_i$ instead of $\boldsymbol{\nabla} C_i$ leads to the same conclusions. In that case, the derivatives of the function A in (10) are such that: $A^{(2k+1)} \equiv 0$ thanks to the symmetry of the kernel and $\left|A^{(2k)}\right| \leq \dfrac{C_k}{R^{2k}}$ where C_k depends on the ratio $R/\Delta x$ and on the choice of the kernel.

3.2. Uniform translation and local rotation invariance

As already mentioned in Section 2.1, the PST introduced by Monaghan has the advantage of being Galilean invariant. This is the second condition that the PST should verify. Moreover, the PST should be the same with or without the presence of rotation at any instant.

The quantity $R\boldsymbol{\nabla} C_i$ (or $R\widehat{\boldsymbol{\nabla}} C_i$) itself is invariant by uniform translation and local rotation. Then, U^{char} and U^{lim} should be chosen properly so that $\boldsymbol{\delta u}$ maintains this nice property. Note that using the local or global Lagrangian particle velocity does not allow these invariance conditions to be fulfilled. Conversely, using a relative velocity such that $U_i^{char} = f(\boldsymbol{u}_j - \boldsymbol{u}_i)$ is a sufficient condition (in situations where the limitation is never reached), and using in addition a similar U_i^{lim} allows the Galilean invariance to be recovered in any case. It is important to note that, conversely to the PST velocities introduced in Tab. 1, U_i^{char} and U_i^{lim} are in this case variable in space and time.

Furthermore, using a first order Taylor's expansion (at location $\boldsymbol{x}_i$ for instance), leads theoretically to:

$$\boldsymbol{u}_j - \boldsymbol{u}_i \approx \overline{\overline{\nabla}} \boldsymbol{u}_{x_i} (\boldsymbol{x}_j - \boldsymbol{x}_i) = O(\Delta x), \tag{17}$$

where $\overline{\overline{\nabla}} \boldsymbol{u}_{x_i}$ is the velocity gradient at $\boldsymbol{x}_i$. Then, basing U_i^{char} and U_i^{lim} on $\boldsymbol{u}_j - \boldsymbol{u}_i$ in the generic PST velocity formulation (8) allows for ensuring both the Galilean invariance and the consistency condition (9) where $\boldsymbol{u} \in \mathcal{C}^1$, with a theoretical first order convergence rate.

In addition, with a projection $(\boldsymbol{u}_j - \boldsymbol{u}_i) \cdot \dfrac{\boldsymbol{x}_j - \boldsymbol{x}_i}{\|\boldsymbol{x}_j - \boldsymbol{x}_i\|}$, the local rotation invariance is obtained.

To summarize, using any of the characteristic (and limitation) velocities proposed in Eqs. (18)-(20) in the generic form (8) allows to fulfill (i) the condition of Galilean and local rotation invariance, (ii) the consistency condition (9).

$$U_i^{char} = \min_{j \in \mathcal{D}_i} \left(\left| \omega_i(j) (\boldsymbol{u}_j - \boldsymbol{u}_i) \cdot \frac{\boldsymbol{x}_j - \boldsymbol{x}_i}{\|\boldsymbol{x}_j - \boldsymbol{x}_i\|} \right| \right), \tag{18}$$

$$U_i^{char} = \overline{\left| \omega_i\left(j\right)\left(\boldsymbol{u}_j - \boldsymbol{u}_i\right) \cdot \frac{\boldsymbol{x}_j - \boldsymbol{x}_i}{\left\|\boldsymbol{x}_j - \boldsymbol{x}_i\right\|} \right|_i}, \tag{19}$$

$$U_i^{char} = \max_{j \in \mathcal{D}_i} \left(\left| \omega_i\left(j\right)\left(\boldsymbol{u}_j - \boldsymbol{u}_i\right) \cdot \frac{\boldsymbol{x}_j - \boldsymbol{x}_i}{\left\|\boldsymbol{x}_j - \boldsymbol{x}_i\right\|} \right| \right), \tag{20}$$

where $\omega_i\left(j\right)$ is a weight function. In this paper, the weight function is taken such that $\omega_i\left(\cdot\right) \equiv 1$ but another function could be chosen to give a stronger weight to the particles j close to the particle i, for instance in order to smooth out U_i^{char} in presence of free-surface reconnection.

3.3. Independence of the PST from the solution

The PST should act with respect to a local measure of the flow dynamics. For example, in a dam-break test case, the maximum Lagrangian velocity is reached in the fluid front, whereas the dynamics of the flow is relatively low elsewhere. In such a case, basing the PST on the maximum Lagrangian velocity U_{max} can lead to an excessive particle shifting in low dynamics region. This last condition proposed aims at avoiding such an undesirable property.

$R\boldsymbol{\nabla} C_i$ (or $R\widehat{\boldsymbol{\nabla}} C_i$) are some local quantities and therefore do not depend on the global behavior of the flow. Note that the characteristic velocities proposed in Eqs. (18)-(20) are independent of any global velocity of the flow and therefore fulfill also the desired local property of the PST.

4. PST enhancements

4.1. Proposition of an improved PST velocity

From the discussion and analysis drawn in Section 3, we derive here the proposition of an enhanced PST. For the particles located inside the fluid (i.e. far from a free-surface or a solid boundary), we propose the following PST velocity:

$$\boldsymbol{\delta u}_i = \alpha \begin{cases} -U_i^{char} \beta_i R \widehat{\boldsymbol{\nabla}} C_i & \text{if } \left\| \beta_i R\, U_i^{char} \widehat{\boldsymbol{\nabla}} C_i \right\| < \dfrac{1}{2} \dfrac{R}{\Delta x} U_i^{lim} \\ -U_i^{lim} \dfrac{1}{2} \dfrac{R}{\Delta x} \dfrac{\widehat{\boldsymbol{\nabla}} C_i}{\left\| \widehat{\boldsymbol{\nabla}} C_i \right\|} & \text{otherwise} \end{cases}, \tag{21}$$

where U_i^{char} and U_i^{lim} are defined as Eq. (20) with the weight function $\omega_i(j) \equiv 1$. $\widehat{\boldsymbol{\nabla}} C_i$ is the pointing vector defined in Eq. (3), β_i is a coefficient introduced to counterbalance the term of lowest degree appearing in Eq. (11), and typically $\beta_i = \left(\dfrac{R}{\Delta x} \right)^3$. Note that the reference to i appearing in β_i is not necessary at this stage, but it will be needed in Section 5 where the PST close to a free-surface is introduced. Lastly, α is a shifting amplitude coefficient fixed to $\alpha = 0.5$ throughout this paper. Theoretically, $R\widehat{\boldsymbol{\nabla}} C_i$ is $O\left(1\right)$ but it is not possible to predict its exact value a priori. To prevent excessive values, a limitation by $\dfrac{1}{2}\dfrac{R}{\Delta x}$ is prescribed. Making these choices, the PST velocity validated in this paper finally reads:

$$\boldsymbol{\delta u}_i = 0.5 \begin{cases} -\max\limits_{j \in \mathcal{D}_i} \left(\left| \left(\boldsymbol{u}_j - \boldsymbol{u}_i\right) \cdot \dfrac{\boldsymbol{x}_j - \boldsymbol{x}_i}{\left\|\boldsymbol{x}_j - \boldsymbol{x}_i\right\|} \right| \right) \left(\dfrac{R}{\Delta x} \right)^3 R \widehat{\boldsymbol{\nabla}} C_i & \text{if } \left\| \left(\dfrac{R}{\Delta x} \right)^3 R \widehat{\boldsymbol{\nabla}} C_i \right\| < \dfrac{1}{2} \dfrac{R}{\Delta x}\,, \\ -\max\limits_{j \in \mathcal{D}_i} \left(\left| \left(\boldsymbol{u}_j - \boldsymbol{u}_i\right) \cdot \dfrac{\boldsymbol{x}_j - \boldsymbol{x}_i}{\left\|\boldsymbol{x}_j - \boldsymbol{x}_i\right\|} \right| \right) \dfrac{1}{2} \dfrac{R}{\Delta x} \dfrac{\widehat{\boldsymbol{\nabla}} C_i}{\left\| \widehat{\boldsymbol{\nabla}} C_i \right\|} & \text{otherwise}\,, \end{cases} \tag{22}$$

whose properties are summarized in Tab. 2. By construction, the proposed PST verifies the targeted conditions introduced in Section 3. Furthermore, another advantage of this PST is its compatibility with the incompressible assumption, thanks to the absence of sound speed terms.

	$\lim_{\Delta x \to 0} \boldsymbol{\delta r} = \mathbf{0}$	$\lim_{\Delta x \to 0} \boldsymbol{\delta u} = \mathbf{0}$	Galilean and local rotation invariance	Independence global flow / local PST	Compatibility with incompressible assumption	PST based on Fick's law
Monaghan [22]	Yes	Yes	Only Galilean	Yes	Yes	No
Lind *et al.* [17]	Yes	if $\frac{\Delta x}{R} \to 0$	No	No	Derived for incompressible	Yes
Oger *et al.* [25]	Yes	if $\frac{\Delta x}{R} \to 0$	No	No	No	Yes
Sun *et al.* [32]	Yes	if $\frac{\Delta x}{R} \to 0$	No	No	No	Yes
Present PST	Yes	Yes	Yes	Yes	Yes	Yes

Table 2: Summary of the theoretical properties of PSTs.

It is important to note that here we mainly focus on PSTs based on Fick's law written through the generic formulation (8). However, it is not the only possibility to build a PST. As an example, Adami *et al.* [1] derived a PST built through the computation of an acceleration, computed as $\frac{\boldsymbol{\nabla} P_b}{\rho}$ where P_b is a background pressure, numerically chosen as $P_b = P_0$, with P_0 the reference pressure. Therefore, this background pressure gives the magnitude of the PST, implying that the consistency condition (9) is not fulfilled. In addition, despite its Galilean invariance property, this PST does not allow for recovering the local rotation invariance and independence from the solution.

4.2. SPH schemes used to validate the present PST

In this work, the PST is validated through different SPH formulations, which are first recalled in the present section. For all these schemes, the system of equations is closed using the Cole equation of state $p = \frac{c_0^2 \rho_0}{\gamma}\left[\left(\frac{\rho}{\rho_0}\right)^\gamma - 1\right]$ where γ, ρ_0 and c_0 are respectively the polytropic constant, reference density and nominal speed of sound. The $\mathcal{C}^2$ Wendland kernel [38] is used with a ratio $R/\Delta x = 4$ in 2D and $R/\Delta x = 3$ in 3D. Finally, time derivatives are integrated using a 4^{th}-order Runge-Kutta scheme, and the time-step is computed through the following CFL condition:

$$\Delta t = CFL \min_i \frac{R_i}{c_0} \tag{23}$$

with R_i the kernel radius associated to the particle i and CFL=0.375

4.2.1. Riemann-based scheme derived from an ALE formalism

Vila [37] derived a weakly-compressible Riemann-based SPH scheme written in ALE formalism. This scheme, then studied for instance in [25] and [29], is rewritten here using a velocity decomposition:

$$\frac{d\boldsymbol{x}_i}{dt} = \boldsymbol{u}_i + \boldsymbol{\delta u}_i \quad , \tag{24}$$

$$\frac{dV_i}{dt} = V_i \sum_{j\in\mathcal{D}_i} (\boldsymbol{u}_j - \boldsymbol{u}_i)\cdot\boldsymbol{\nabla}_i W_{ij}\ V_j + V_i \sum_{j\in\mathcal{D}_i} (\boldsymbol{\delta u}_j - \boldsymbol{\delta u}_i)\cdot\boldsymbol{\nabla}_i W_{ij}\ V_j \quad , \tag{25}$$

$$\frac{d\left(V_i\rho_i\right)}{dt} = -V_i \sum_{j\in\mathcal{D}_i} 2\rho_E\left(\boldsymbol{u}_E - \boldsymbol{u}_{ij}\right)\cdot\boldsymbol{\nabla}_i W_{ij}\ V_j + V_i \sum_{j\in\mathcal{D}_i} \rho_E\left(\boldsymbol{\delta u}_i + \boldsymbol{\delta u}_j\right)\cdot\boldsymbol{\nabla}_i W_{ij} V_j \quad , \tag{26}$$

$$\frac{d\left(V_i\rho_i\boldsymbol{u}_i\right)}{dt} = \underbrace{\begin{array}{l}-V_i \sum_{j\in\mathcal{D}_i} 2\left[\rho_E\boldsymbol{u}_E\otimes\left(\boldsymbol{u}_E - \boldsymbol{u}_{ij}\right) + P_E\mathbb{I}\right]\boldsymbol{\nabla}_i W_{ij}\ V_j \\ +V_i\rho_i\boldsymbol{g}\end{array}}_{\text{Lagrangian part}} + \underbrace{V_i \sum_{j\in\mathcal{D}_i} \left[\rho_E\boldsymbol{u}_E\otimes\left(\boldsymbol{\delta u}_i + \boldsymbol{\delta u}_j\right)\right]\boldsymbol{\nabla}_i W_{ij} V_j}_{\text{PST part}} \quad , \tag{27}$$

with $\boldsymbol{u}_{ij} = \dfrac{\boldsymbol{u}_i + \boldsymbol{u}_j}{2}$, $\mathbb{I}$ the identity matrix and $\boldsymbol{g}$ the gravity. ρ_E, $\boldsymbol{u}_E$ and P_E are the Riemann problem solutions at the interface between particles i and j which is supposed to be located at the $i-j$ mid-distance $\boldsymbol{x}_{ij}$ and moving at the velocity $\boldsymbol{u}_{0ij} = \dfrac{\boldsymbol{u}_{0i} + \boldsymbol{u}_{0j}}{2}$ with $\boldsymbol{u}_0 = \boldsymbol{u} + \boldsymbol{\delta u}$. The MUSCL scheme [36] with the minmod slope limiter [30] is used to reconstruct the conservative variables $\begin{pmatrix}\rho \\ \rho\boldsymbol{u}\end{pmatrix}$ at $\boldsymbol{x}_{ij}$ for an increased accuracy.

4.2.2. Riemann-based scheme with PST velocity in the motion equation only

The second SPH scheme studied in this paper was firstly derived by Parshikov & Medin [26] in a Lagrangian framework (i.e. without PST). In [15], the Vila scheme was adapted to two phase flows by canceling the mass fluxes between particles, and the scheme initially derived by Parshikov & Medin was thus recovered. The only difference with [26] resides in the continuity equation which was written with density terms instead of volume terms in [15], those two formulations being strictly equivalent. In this scheme, the stabilization is also performed using a Riemann solver combined with MUSCL reconstructions.

Here, the PST is taken into account in the motion equation exclusively, which reads:

$$\frac{d\boldsymbol{x}_i}{dt} = \boldsymbol{u}_i + \boldsymbol{\delta u}_i \quad , \tag{28}$$

$$\frac{dV_i}{dt} = V_i \sum_{j\in\mathcal{D}_i} 2\left(\boldsymbol{u}_E - \boldsymbol{u}_i\right)\cdot\boldsymbol{\nabla}_i W_{ij}\ V_j \quad , \tag{29}$$

$$\frac{d\left(V_i\rho_i\right)}{dt} = 0 \quad , \tag{30}$$

$$\frac{d\left(V_i\rho_i\boldsymbol{u}_i\right)}{dt} = \underbrace{-V_i \sum_{j\in\mathcal{D}_i} 2P_E\boldsymbol{\nabla}_i W_{ij}\ V_j + V_i\rho_i\boldsymbol{g}}_{\text{Lagrangian part}} \quad \underbrace{}_{\text{PST part}} \quad . \tag{31}$$

4.2.3. δ-SPH scheme with PST velocity in the motion equation only

The third SPH scheme used in this work is the δ-SPH scheme, firstly derived in [3, 18]:

$$\frac{d\boldsymbol{x}_i}{dt} = \boldsymbol{u}_i + \boldsymbol{\delta u}_i \quad , \tag{32}$$

$$\frac{d\rho_i}{dt} = -\rho_i \sum_{j\in\mathcal{D}_i} (\boldsymbol{u}_j - \boldsymbol{u}_i)\cdot\boldsymbol{\nabla}_i W_{ij}\ V_j + \Pi_{i,\delta}^{(\rho)} \quad , \tag{33}$$

$$\frac{d\left(V_i\rho_i\right)}{dt} = 0 \quad , \tag{34}$$

$$\rho_i\frac{d\boldsymbol{u}_i}{dt} = \underbrace{\sum_{j\in\mathcal{D}_i} \left(P_i + P_j\right)\boldsymbol{\nabla}_i W_{ij}\ V_j + \boldsymbol{\Pi}_{i,\delta}^{(\boldsymbol{u})} + V_i\rho_i\boldsymbol{g}}_{\text{Lagrangian part}} \quad \underbrace{}_{\text{PST part}} \quad . \tag{35}$$

where the diffusive terms $\Pi_{i,\delta}^{(\rho)}$ and $\mathbf{\Pi}_{i,\delta}^{(\boldsymbol{u})}$ are:

$$\Pi_{i,\delta}^{(\rho)} = \delta h c_0 \sum_{j\in\mathcal{D}_i} \boldsymbol{\psi_{ij}} \cdot \boldsymbol{\nabla}_i W_{ij} V_j \ , \ \text{with } \boldsymbol{\psi_{ij}} = 2(\rho_j - \rho_i)\frac{\boldsymbol{x}_{ij}}{||\boldsymbol{x}_{ij}||^2} - [\langle\boldsymbol{\nabla}\rho\rangle_i^{\mathcal{L}} + \langle\boldsymbol{\nabla}\rho\rangle_j^{\mathcal{L}}] \ , \tag{36}$$

$$\mathbf{\Pi}_{i,\delta}^{(\boldsymbol{u})} = \alpha h c_0 \rho_0 \sum_{j\in\mathcal{D}_i} \pi_{ij} \boldsymbol{\nabla}_i W_{ij} V_j \ , \ \text{with } \pi_{ij} = \frac{(\boldsymbol{u}_j - \boldsymbol{u}_i)\cdot(\boldsymbol{x}_j - \boldsymbol{x}_i)}{||\boldsymbol{x}_{ij}||^2} \ , \tag{37}$$

with $\alpha = 0.01$ and $\delta = 0.1$ in the present work unless otherwise specified.

4.3. Validation of the PST consistency

4.3.1. Case of an inviscid flow

This section aims at verifying the validity in 2D of the consistency property (9) studied theoretically in 1D so far. To this end, 2D Taylor-Green vortices for an inviscid flow [35] are considered, the PST being crucial in this test case [2, 25]. The initial velocity and pressure are given by:

$$u_x^* = \sin(2\pi x^*)\cos(2\pi y^*) \ , \tag{38}$$

$$u_y^* = -\cos(2\pi x^*)\sin(2\pi y^*) \ , \tag{39}$$

$$p^* = \frac{1}{2}\left[\cos(4\pi x^*) + \cos(4\pi y^*)\right] \ , \tag{40}$$

in the square shaped fluid domain of size $[0, L] \times [0, L]$. The superscript * stands for the dimensionless variables with the reference length L, velocity U, time L/U and pressure $\frac{\rho U^2}{2}$, being U the maximum velocity in the initial condition. In this case, the nominal sound speed is taken as $c_0 = 10 \times U$.

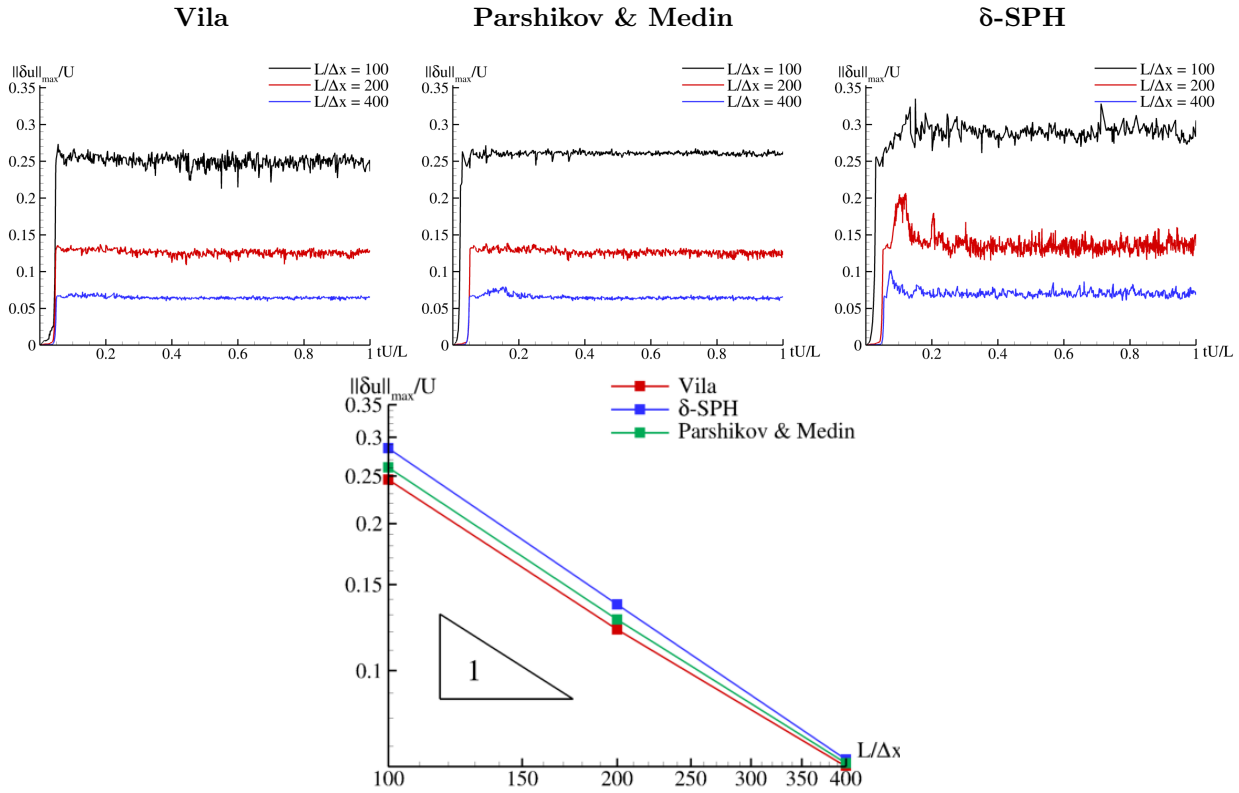

Figure 1: Inviscid 2D Taylor-Green vortices. Top: time evolution of the maximum PST velocity $\|\boldsymbol{\delta u}\|_{max}$ for three spatial resolutions. Left: Vila scheme. Middle: Parshikov & Medin scheme. Right: δ-SPH scheme. Bottom: convergence rate of $\|\boldsymbol{\delta u}\|_{max}$ for the three SPH schemes tested.

Fig. 1 shows the time evolution of the maximum PST velocity $\|\boldsymbol{\delta u}\|_{max}$ for three different spatial resolutions and with the three SPH schemes tested. We observe that the property (9) is verified numerically for all the SPH schemes tested here. Moreover, the theoretical first order of convergence is retrieved. In Fig. 2, the pressure field is plotted at different time instants of the simulation for the Vila scheme. While the initial configuration is Cartesian, we observe that the coherent structures start breaking from the very beginning of the simulation, and the PST introduced in this paper succeeds in suppressing all of them without altering the pressure field. When using the finest resolution, we can see in Fig. 3 that the PST is efficient for the three schemes studied in this paper despite the small values of $\boldsymbol{\delta u}$. Note that a deviation of the pressure values occurs for the SPH schemes in which the PST is taken into account in the motion equation only, i.e. δ-SPH and Parshikov & Medin. Nevertheless, this wrong effect should be imputed to the absence of $\boldsymbol{\delta u}_i$ terms in the mass and momentum equations within these SPH formulations, rather than to the PST itself. As a matter of fact, Colagrossi *et al.* [7] and Sun *et al.* [32] recently proposed alternative formulations of the δ-SPH scheme to answer this issue, and we have also developed Riemann-based formulations for which the theoretical results are retrieved [20].

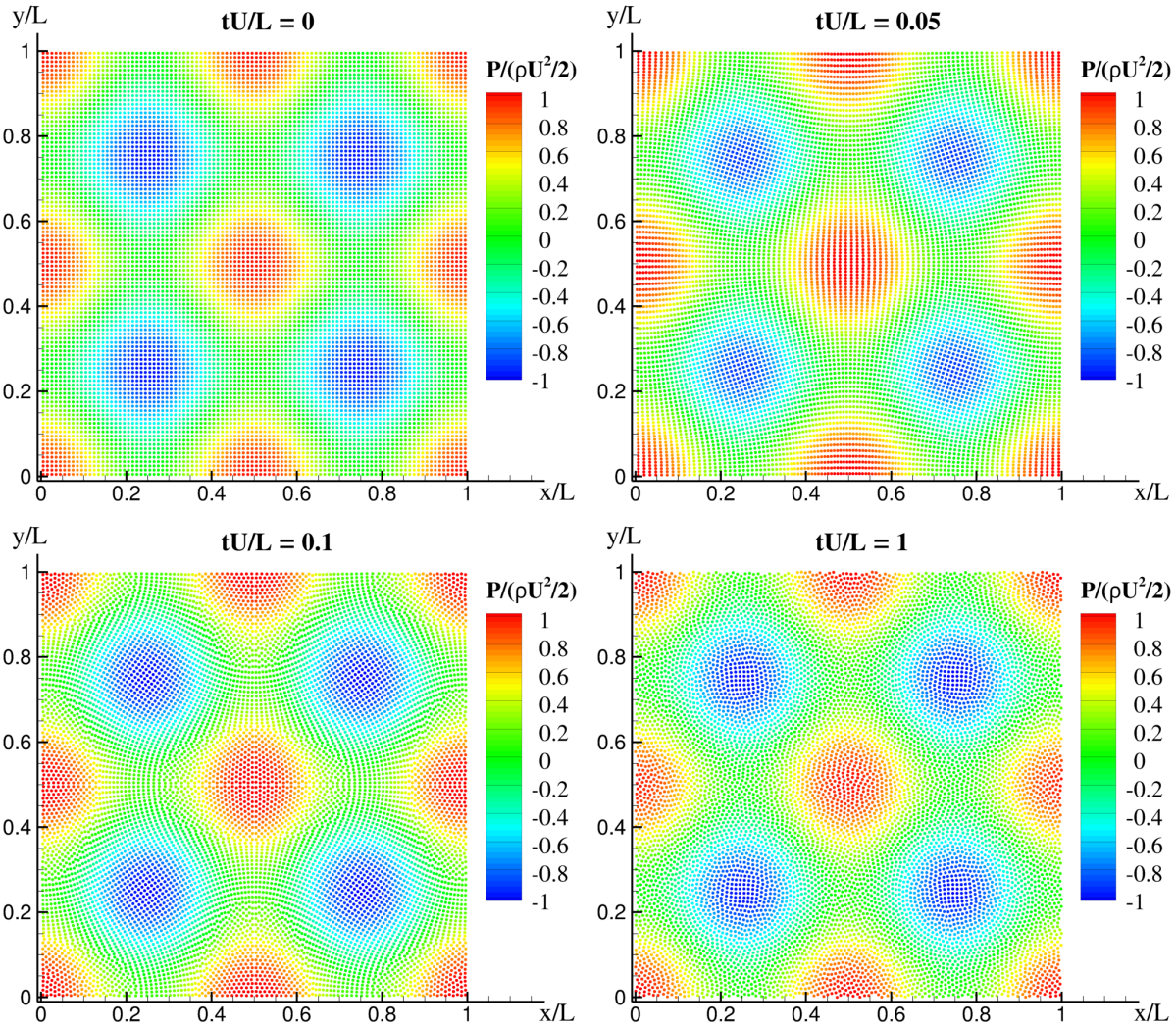

Figure 2: Inviscid 2D Taylor-Green vortices. Pressure field obtained with the Vila scheme and $L/\Delta x = 100$ at $tU/L = 0$, $tU/L = 0.05$, $tU/L = 0.1$ and $tU/L = 1$.

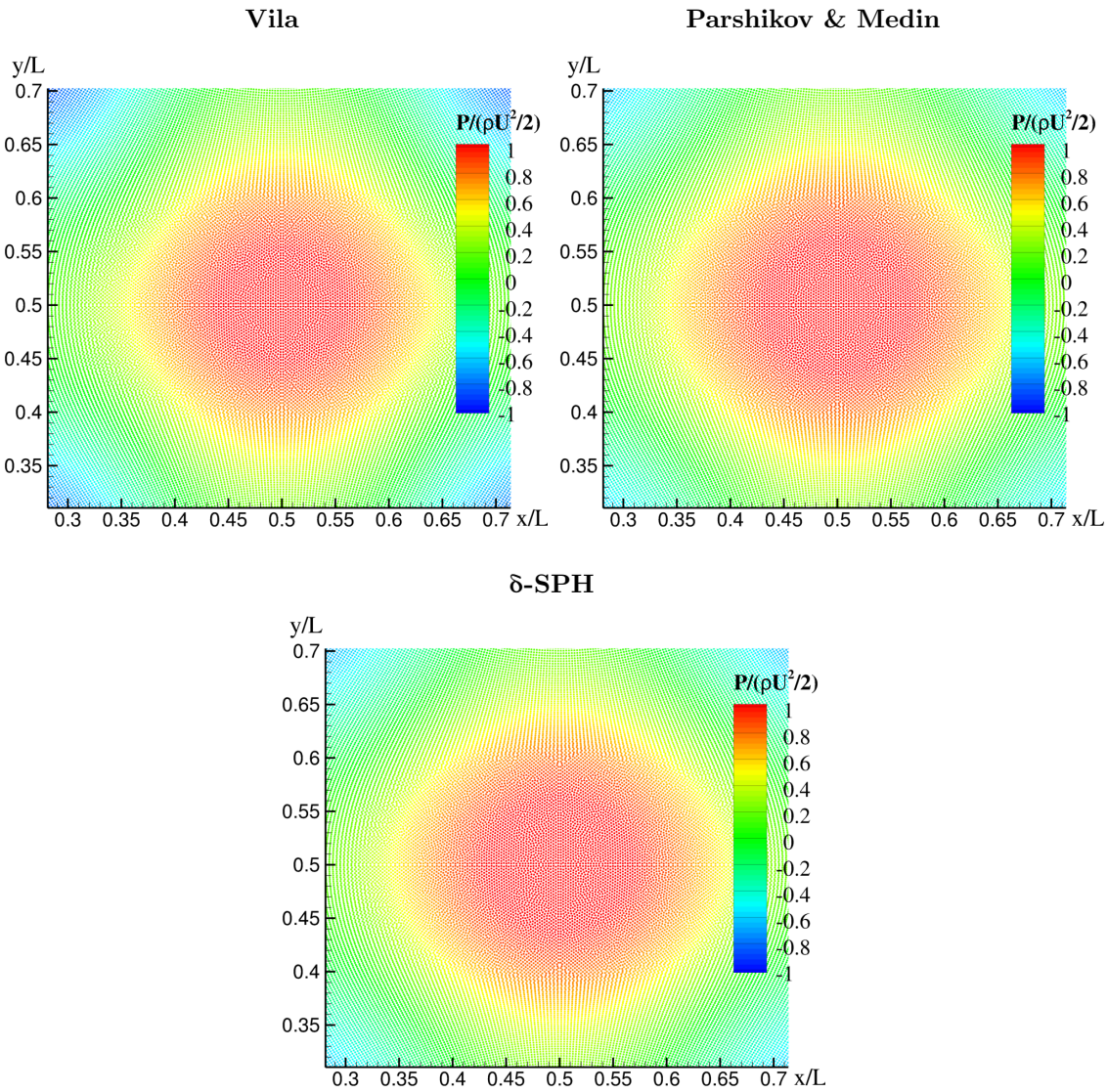

Figure 3: Inviscid 2D Taylor-Green vortices. Pressure field at $tU/L = 0.1$ with $L/\Delta x = 400$. Zoom in the center of the square. Left: Vila scheme. Right: Parshikov & Medin scheme. Bottom: δ-SPH scheme.

We check here the gain in the numerical dissipation provided by the PST, through the analysis of the kinetic energy decay. Fig. 4 shows that the dissipation tends towards zero while increasing the spatial resolution for the three schemes studied. Note that we aim here at showing that the PST has the same effect on the numerical diffusion whatever the SPH scheme used, and not to compare the diffusion properties of these schemes. For instance, the δ-SPH scheme would display a lower dissipation by using a smaller diffusion coefficient.

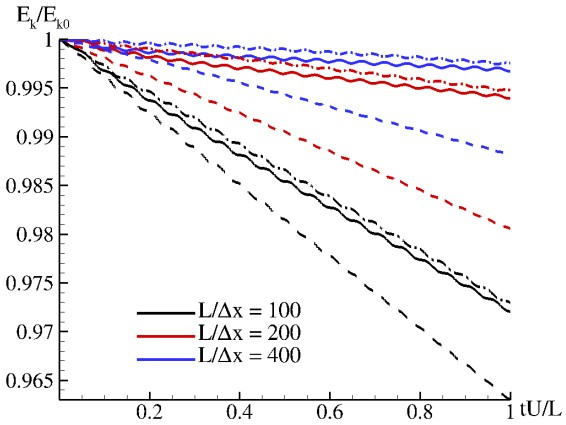

Figure 4: Inviscid 2D Taylor-Green vortices. Kinetic energy decay for three spatial resolutions. Solid: Vila scheme. Dot-dashed: Parshikov & Medin scheme. Dashed: δ-SPH scheme.

4.3.2. Case of a viscous flow

We propose here to validate the proposed PST for a viscous flow. To this end, the Taylor-Green vortices at Reynolds number $Re = 100$ are considered (see e.g. [25] for more details). For the three schemes tested, the viscous part is discretized using the Monaghan & Gingold operator [24]. Note that, for the δ-SPH scheme (32)-(35), the artificial viscosity is here replaced by the physical viscosity, meaning that $\alpha = 0$ in (37), as proposed in [33] for example.

Because of the presence of viscous terms, the following CFL condition is used for the three schemes tested:

$$\Delta t = \min\left(CFL_\nu \min_i \frac{R_i^2}{\nu}, CFL \min_i \frac{R_i}{c_0}\right), \tag{41}$$

where ν is the dynamic viscosity, $CFL_\nu = 0.025$, and $CFL = 0.375$ as in Eq. (23).

In Fig. 5, the maximum PST velocity is plotted for three spatial resolutions and for the three schemes tested. We have also represented in green dashed lines the theoretical values corresponding to a first order of convergence at three instants of the simulation. As we can observe, due to the presence of the viscosity, the maximum PST velocity decreases over time in all the simulations. In addition, for the three schemes tested, the maximum PST converged while refining the spatial resolution, and the first order of convergence seems to be recovered all along the simulation. Regarding the kinetic energy, a good agreement with the analytical solution is found for the three SPH schemes tested, as observed in Fig. 6. Note that (i) for the Vila scheme, the convergence is obtained from $L/\Delta x = 200$ and the solution is very close the analytical one, (ii) for the δ-SPH scheme the solution is converged from $L/\Delta x = 100$ with a small gap in comparison to the analytical solution.

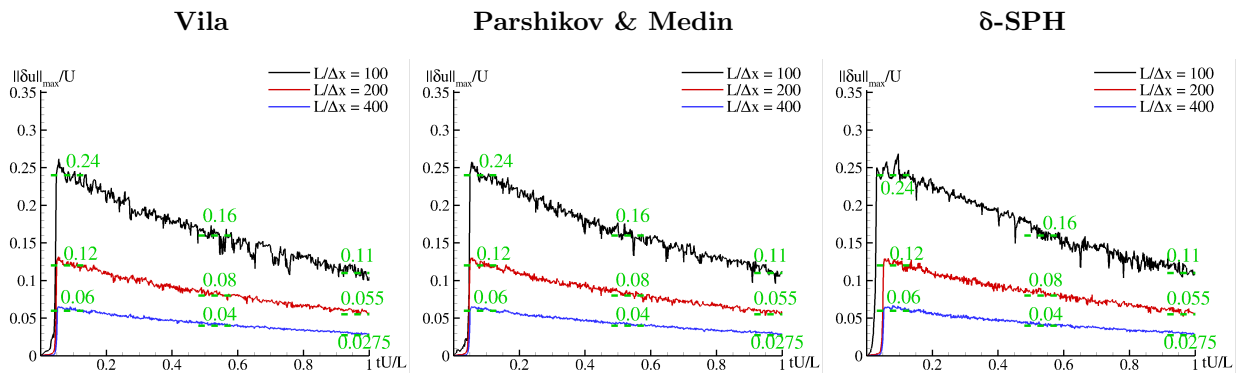

Figure 5: 2D Taylor-Green vortices at $Re = 100$. Time evolution of the maximum PST velocity $\|\boldsymbol{\delta u}\|_{max}$ for three spatial resolutions. Left: Vila scheme. Middle: Parshikov & Medin scheme. Right: δ-SPH scheme. The values of the theoretical first order convergence at three specific instants are plotted in green dashed line on each figure.

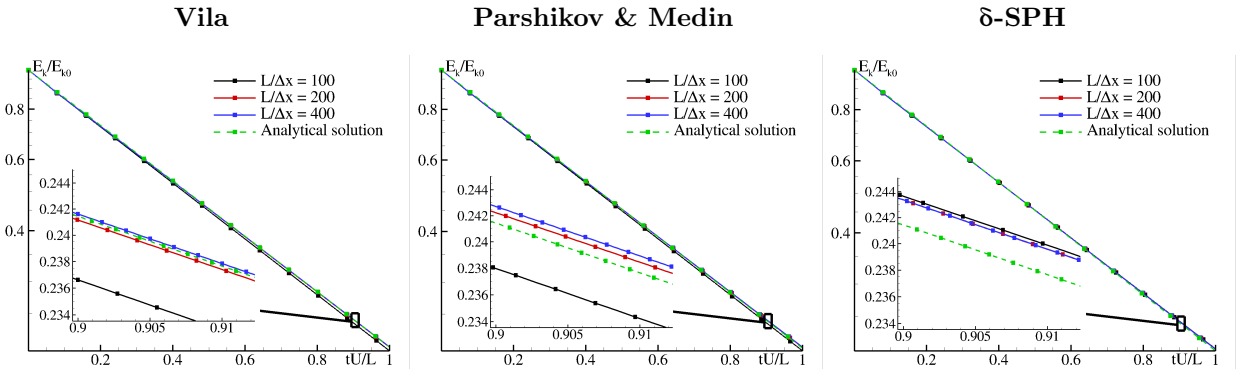

Figure 6: 2D Taylor-Green vortices at $Re = 100$. Time evolution of the kinetic energy for three spatial resolutions. The analytical solution is also provided. Left: Vila scheme. Middle: Parshikov & Medin scheme. Right: δ-SPH scheme.

4.4. Validation of uniform translation invariance

In order to check the Galilean invariance property, the Taylor-Green test case is still considered here, but the initial configuration is modified by adding a translation velocity $U^0 = 2U$ in Eq. (38) (where U is the maximum velocity of the original case).

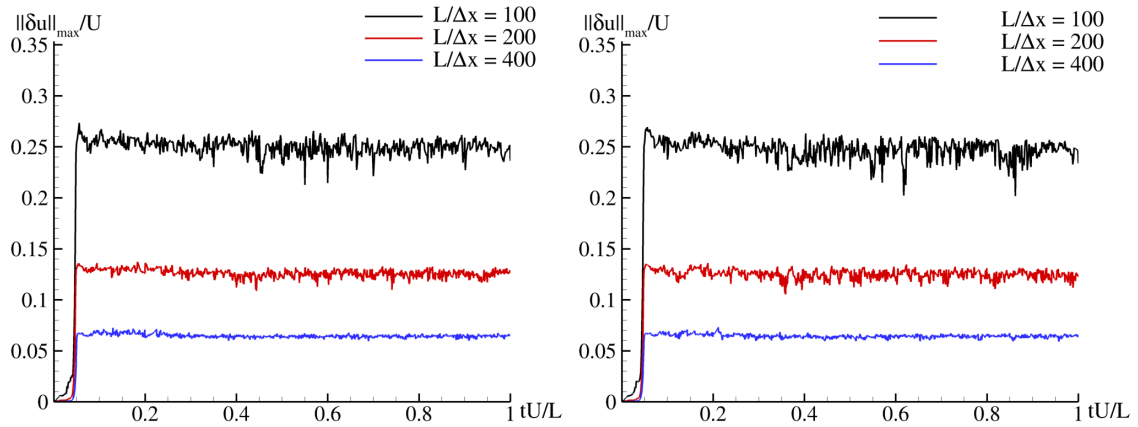

Figure 7: Inviscid 2D Taylor-Green vortices. Time evolution of the maximum PST velocity $\|\boldsymbol{\delta u}\|_{max}$ obtained with the Vila scheme for three spatial resolutions. Left: original Taylor-Green. Right: Taylor-Green with uniform translation.

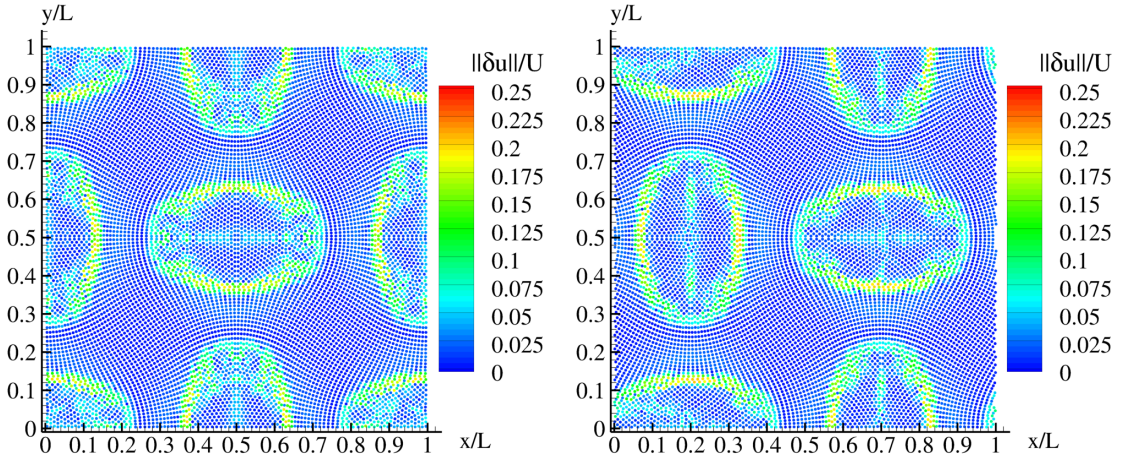

Figure 8: Inviscid 2D Taylor-Green vortices. Distribution of the PST velocity $\|\boldsymbol{\delta u}\|$ at $tU/L = 0.1$ obtained with the Vila scheme with $L/\Delta x = 100$. Left: original Taylor-Green. Right: Taylor-Green with uniform translation.

As visible in Fig. 7, whatever the spatial resolution used there is no major differences in the maximum PST velocity while considering uniform translation or not. Moreover, although small differences can be noticed, the PST velocity remains globally unchanged (see Fig. 8). Regarding the kinetic energy decay (see Fig. 9 in which the contribution of the uniform translation has been subtracted), results are similar with and without applying the uniform translation. Note that these results refer to the Vila scheme but the conclusions are the same when using the other SPH schemes.

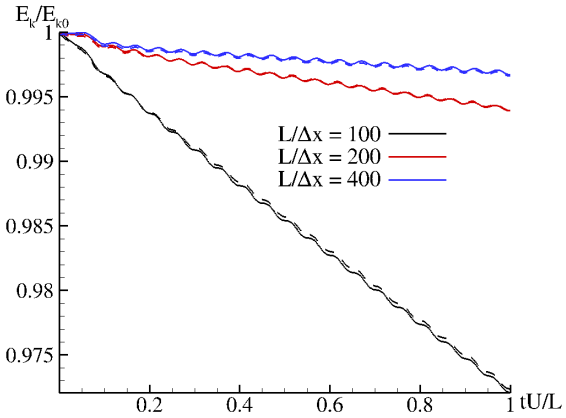

Figure 9: Inviscid 2D Taylor-Green vortices. Kinetic energy decay for three spatial resolutions using the Vila scheme. Solid: original Taylor-Green. Dashed: Taylor-Green with uniform translation.

4.5. Comparison with PSTs of the literature

In this section, we propose to compare the PSTs of Tab. 2 numerically. To this end, the Taylor-Green vortices test case introduced in Section 4.3.1 is considered and the study is performed using the Vila scheme. The choice of this particular scheme to conduct the comparison is due to (i) the fact that some PSTs of Tab. 2 do not theoretically fulfill the consistency condition, and an ALE scheme is theoretically suitable to deal with any arbitrary velocity, and (ii) among the SPH schemes used in this paper, the Vila scheme is the only one for which there is no deviation of the pressure field, allowing then to compare the pressure field obtained for each PST to the analytical solution.

In Tab. 2, we outlined that the PST of Monaghan fulfills almost all the targeted conditions asked for a PST, and in particular the consistency condition. Nevertheless, as we can observe in the left part of Fig. 10, this condition is not recovered numerically. Furthermore, among the PSTs studied in the present paper, the PST of Monaghan is the only one which is not based on Fick's law. As we can see in the right part of Fig. 10, anisotropic distribution of particles remains in the simulation, which deteriorates the obtained solution.

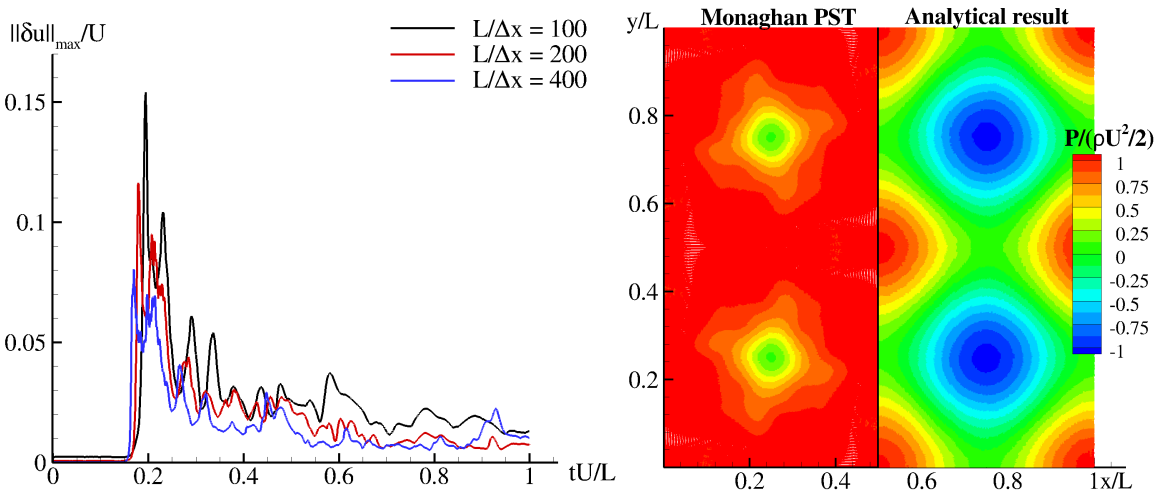

Figure 10: Inviscid 2D Taylor-Green vortices. Results obtained with the Vila scheme and the PST of Monaghan. Left: time evolution of the maximum PST velocity. Right: Pressure field obtained for the spatial resolution $L/\Delta x = 400$ at $tU/L = 0.25$. The analytical pressure field is represented in the right-hand side.

Regarding the PSTs based on Fick's law of Tab. 2, the maximum PST velocity is plotted in Fig. 11. As expected, the consistency condition (9) is not fulfilled, except for the PST derived in this paper. Furthermore, as shown in Fig. 12, the pressure field obtained with the present PST is closer to the reference solution than with the other PSTs. More quantitatively, the maximum error on the pressure values is plotted in Fig. 13 for $L/\Delta x = 400$. We can observe that both the average value and the amplitude of the error are lower with the present PST than with the others, showing the superiority of the present PST on this test case.

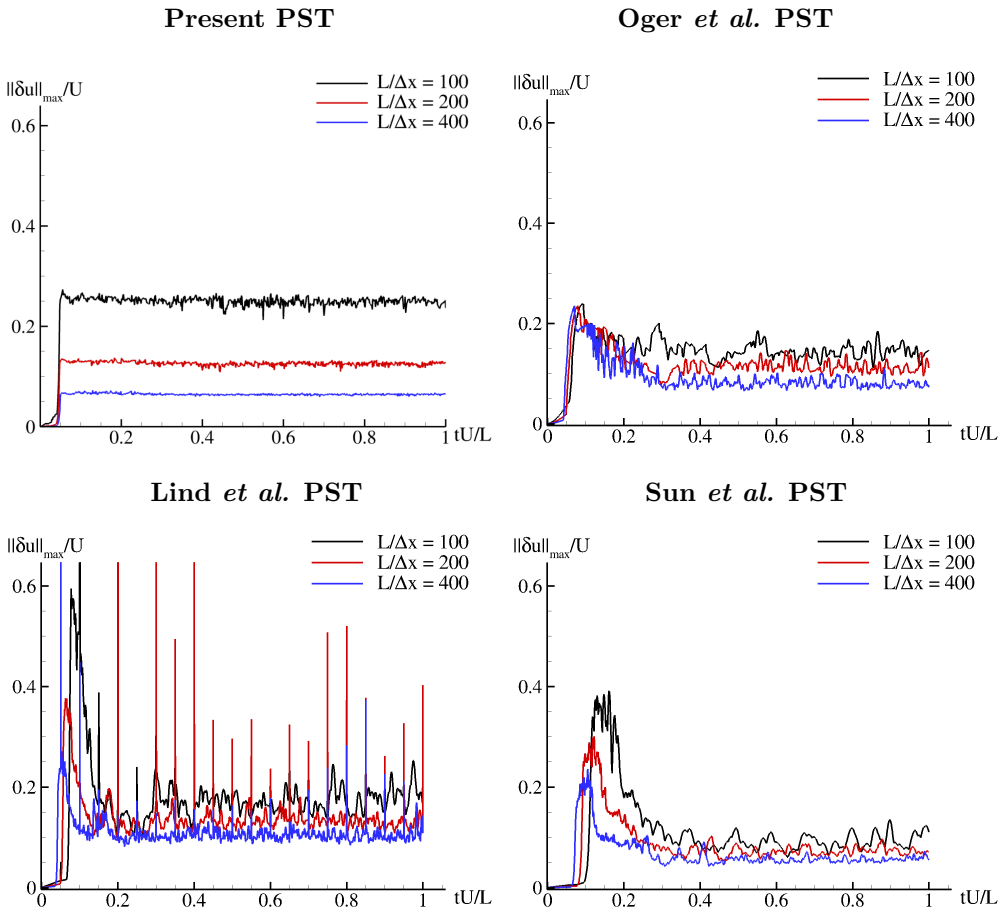

Figure 11: Inviscid 2D Taylor-Green vortices. Time evolution of the maximum PST velocity obtained with the Vila scheme and PSTs based on Fick's law for three spatial resolutions. Top left: Present PST. Top right: Oger *et al.* PST. Bottom left: Lind *et al.* PST. Bottom right: Sun *et al.* PST.

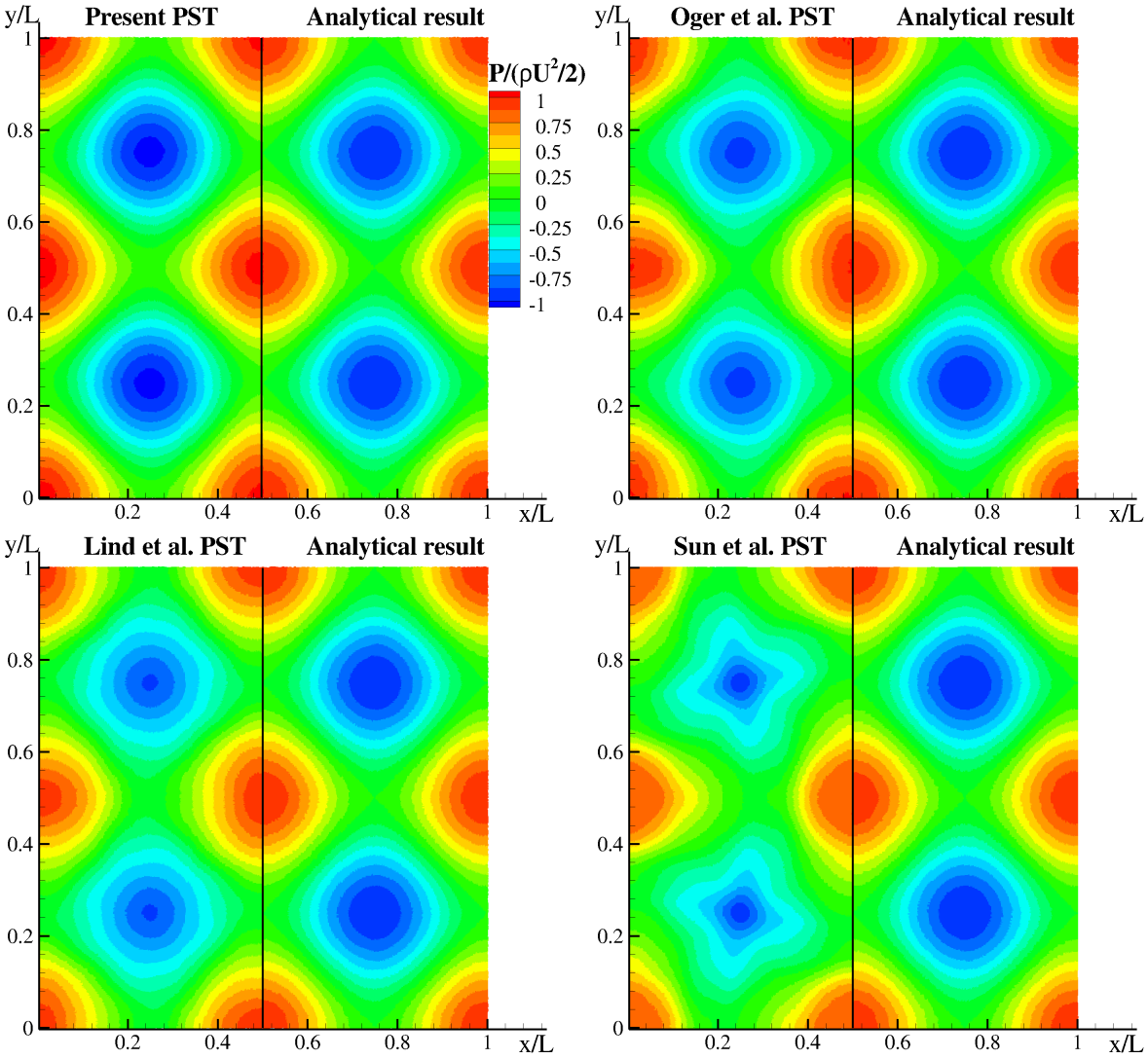

Figure 12: Inviscid 2D Taylor-Green vortices. Pressure field obtained with the Vila scheme for the spatial resolution $L/\Delta x = 400$ at $tU/L = 0.25$ for the present PST (top left), the PST of Oger *et al.* (top right), the PST derived from Lind *et al.* (bottom left), and the PST of Sun *et al.* (bottom right). In each plot, the analytical pressure field is represented in the right-hand side.

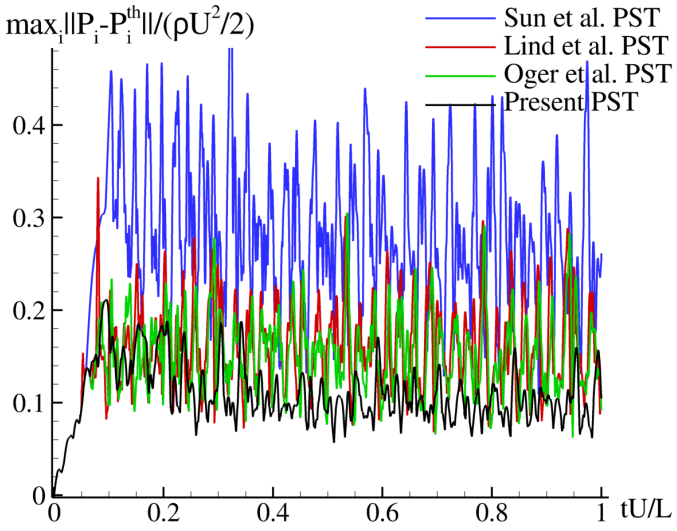

Figure 13: Inviscid 2D Taylor-Green vortices. Time evolution of the maximum error on the pressure values obtained with the Vila scheme with the spatial resolution $L/\Delta x = 400$. The results obtained for the four PSTs based on Fick's law of Tab. 2 are plotted.

5. PST in presence of a free-surface

5.1. Free-surface detection and normal vector

A special attention has been paid recently to the PST close to a free-surface, both in the incompressible context [11, 17] and in the weakly-compressible context [32, 33]. The methodology used to perform a PST in such a region can be divided into two parts (i) detect correctly the free-surface (ii) cancel accurately the normal component of the PST velocity close to the free-surface, in order to maintain the respect of the kinematic condition. The terminology used throughout this paper regarding the free-surface is summarized in Fig. 14.

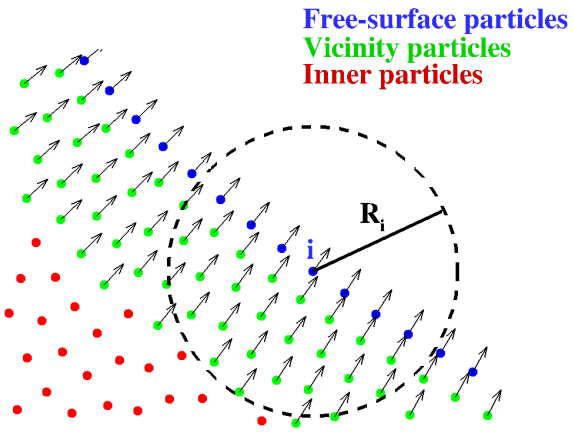

Figure 14: Definition of the free-surface region (defined by the blue and green particles) and the normal vector to the free-surface, here with a ratio $R/\Delta x = 4$.

The free-surface detection algorithm from Marrone *et al.* [19] is commonly used in the SPH community. The first step of this algorithm consists in calculating the minimum eigenvalue (λ_i) of the renormalization matrix [28] defined as:

$$\mathbb{L}_i = \left(\sum_{j \in \mathcal{D}_i} (\boldsymbol{x}_j - \boldsymbol{x}_i) \otimes \boldsymbol{\nabla}_i W_{ij} V_j \right)^{-1} . \tag{42}$$

Then the particles for which $\lambda_i < 0.2$ are considered as free-surface particles while the particles displaying $\lambda_i > 0.75$ are inner particles. For $0.2 < \lambda_i < 0.75$, a second step should be performed to distinguish the free-surface particles from the inner particles: the so-called ice-cream algorithm (see [19] for more details). Once the free-surface particles detected, the free-surface region corresponds to these particles in addition of their neighboring particles (located inside the free-surface particle kernel supports), as schematized in Fig. 14.

In order to cancel the normal component of the PST, the normal vector to the free-surface has to be computed everywhere in the free-surface region. In [19, 11] this vector is evaluated through:

$$\boldsymbol{n}_i = -\frac{\mathbb{L}_i \boldsymbol{\nabla} C_i}{\| \mathbb{L}_i \boldsymbol{\nabla} C_i \|} , \tag{43}$$

while the formulation (44) is preferred in [33, 32] in order to obtain a better accuracy for the particles located far from the free-surface.

$$\boldsymbol{n}_i^{\lambda} = -\frac{\langle \boldsymbol{\nabla} \lambda_i \rangle}{\| \langle \boldsymbol{\nabla} \lambda_i \rangle \|}, \qquad \langle \boldsymbol{\nabla} \lambda_i \rangle = \sum_{j \in \mathcal{D}_i} (\lambda_j - \lambda_i) \, \mathbb{L}_i \boldsymbol{\nabla}_i W_{ij} V_j . \tag{44}$$

In return, an additional CPU time is needed to compute $\langle \boldsymbol{\nabla} \lambda_i \rangle$.

5.2. Theoretical study of $\boldsymbol{\nabla} C_i$ in presence of a free-surface

The expression for the truncation error (10) is valid wherever the kernel support is filled with particles. However, for the particles in the free-surface region, the kernel support is truncated. For a particle located at the free-surface, for which the kernel support is half filled, the truncation error for the gradient of a function A becomes (see Appendix for the details):

$$\begin{aligned} \sum_{j \in \mathcal{D}_i/2} A_j \boldsymbol{\nabla}_i W_{ij} V_j - A_i' = \frac{A_i}{R} \left[O(1) + \xi O\left(\frac{\Delta x}{R}\right) + \frac{1}{2}\left(\xi^2 + \frac{1}{12}\right) O\left(\left(\frac{\Delta x}{R}\right)^2\right) \right] \\ + A_i' \left[O(1) + \xi O\left(\frac{\Delta x}{R}\right) + O\left(\left(\frac{\Delta x}{R}\right)^2\right) \right] \\ + A_i'' R \left[\xi O\left(\frac{\Delta x}{R}\right) + O\left(\left(\frac{\Delta x}{R}\right)^2\right) \right] + \dots , \end{aligned} \tag{45}$$

where $\mathcal{D}_i/2$ stands for the half-filled kernel support. Therefore the approximation of $\boldsymbol{\nabla} C_i$ becomes:

$$\boldsymbol{\nabla} C_i = \sum_{j \in \mathcal{D}_i/2} \boldsymbol{\nabla}_i W_{ij} V_j = \frac{1}{R} \left[O(1) + \xi O\left(\frac{\Delta x}{R}\right) + \frac{1}{2}\left(\xi^2 + \frac{1}{12}\right) O\left(\left(\frac{\Delta x}{R}\right)^2\right) \right] . \tag{46}$$

Hence, the conclusions drawn inside the fluid still hold for the particles located at the free-surface. Note that the term of lowest degree is $O(1)$ in Eq. (46) whereas it is $O\left(\left(\frac{\Delta x}{R}\right)^3\right)$ inside the fluid (see Eq. (11)). Therefore, another conclusion can be made in the presence of a free-surface: $R\boldsymbol{\nabla} C_i$ is $O(1)$ even if $\frac{\Delta x}{R} \to 0$.

5.3. Proposition of a PST in presence of a free-surface

Following the idea of Sun *et al.* [33, 32] and Khayyer *et al.* [11], in this paper the normal component of the PST velocity is progressively canceled in the free-surface region. To preserve an accurate determination of the normal vector far from the free-surface without computing Eq. (44), the following compromise is made: (i) for the free-surface particles the normal vector is determined using (43), (ii) the normal vector of particles in the free-surface region is set equal to the one of their closest free-surface particle neighbor (see Fig. 14). To summarize, this vector noted $\tilde{\boldsymbol{n}}_i$ is defined as:

$$\tilde{\boldsymbol{n}}_i = \begin{cases} \boldsymbol{n}_i & \text{if } i \text{ is a free-surface particle} \\ \boldsymbol{n}_j \quad \text{with } d_i^j = d_i^{FS} & \text{if } i \text{ is a vicinity particle} \end{cases}, \tag{47}$$

where d_i^j is the distance between the particles i and j and d_i^{FS} is the distance between the particle i and its closest free-surface particle neighbor. The PST proposed in this paper (inspired from Sun *et al.* [33, 32] with some slight modifications to account for the PST velocity proposed) is then processed as follows:

- In order to counterbalance the term of lowest degree appearing in Eqs. (11) and (46), the coefficient β_i in Eq. (21) is modified such that $\beta_i = (R/\Delta x)^3$ for the inner particles with a linear decreasing in the free-surface region to reach $\beta_i = 1$ for the free-surface particles.
- For any particle i in the free-surface region, if $\lambda_i < 0.4$ corresponding to regions of low number of neighbors, the PST velocity is set to $\boldsymbol{\delta u}_i = \boldsymbol{0}$.
- For a particle i in the free-surface region, such that $\lambda_i \geq 0.4$ and $d_i^{FS} \leq R/2$, the normal component of $\boldsymbol{\delta u}_i$ is totally canceled.
- For a particle i in the vicinity of the free-surface, with $\lambda_i \geq 0.4$ and $d_i^{FS} > R/2$, the normal component of $\boldsymbol{\delta u}_i$ is gradually permitted.
- No restriction regarding the PST velocity direction is imposed to inner particles.

Finally, the coefficient λ_i^2 is applied to limit the PST magnitude close to the free-surface. Explicitly, the PST in the free-surface region reads:

$$\boldsymbol{\delta u}_i^{FS} = \begin{cases} \boldsymbol{0} & \text{if } \lambda_i < 0.4 \\ \lambda_i^2 \left(\boldsymbol{\delta u}_i - \sigma_i \left(\boldsymbol{\delta u}_i \cdot \widetilde{\boldsymbol{n}}_i \right) \widetilde{\boldsymbol{n}}_i \right) & \text{otherwise} \end{cases}, \tag{48}$$

where $\sigma_i = \min\left[1, \max\left(0, \dfrac{d_i^{FS} - R}{R/2 - R}\right)\right]$ and with $\boldsymbol{\delta u}_i$ as defined in (21) with the modification brought regarding the coefficient β_i.

Note that the modifications made to the PST to account for the free-surface do not affect neither the Galilean and local rotation invariance nor the independence of the PST from the solution. Moreover, an additional consistency property is ensured at the free-surface, as outlined in Tab. 3.

	$\lim_{\Delta x \to 0} \boldsymbol{\delta u}^{FS} = \mathbf{0}$
Lind *et al.* [17]	No
Oger *et al.* [25]	No
Sun *et al.* [32]	No
Present PST	Yes

Table 3: Summary of the theoretical properties of PSTs based on Fick's law in presence of a free-surface.

5.4. Validation of the PST in presence of a free-surface

To validate the proposed PST in the presence of a free-surface, the rotation of an initially square patch of fluid is considered [14]. The velocity of the square patch of length L is initialized using $\boldsymbol{u}^0(x, y) = (\omega y, -\omega x)$ where ω is a constant angular velocity. The pressure is initialized with the hypothesis of an incompressible flow by solving a Poisson equation. During the first tests with $c_0 = 10U_{max}$ (U_{max} being the maximum velocity), a transfer from the compressible energy to the kinetic one was noticed at the very beginning of the simulation, probably due to the difference between incompressible initialization and weakly-compressible assumption. Using fine spatial resolutions (typically from $L/\Delta x = 800$) for which the numerical diffusion is very small, perturbations were then observed at the free-surface. Therefore, the simulations are performed here using $c_0 = 40U_{max}$ to limit the difference between incompressible initialization and weakly-compressible assumption, unless otherwise specified. The reference length, velocity, time and pressure are respectively the square length L, ωL, $1/\omega$ and $\rho(\omega L)^2$.

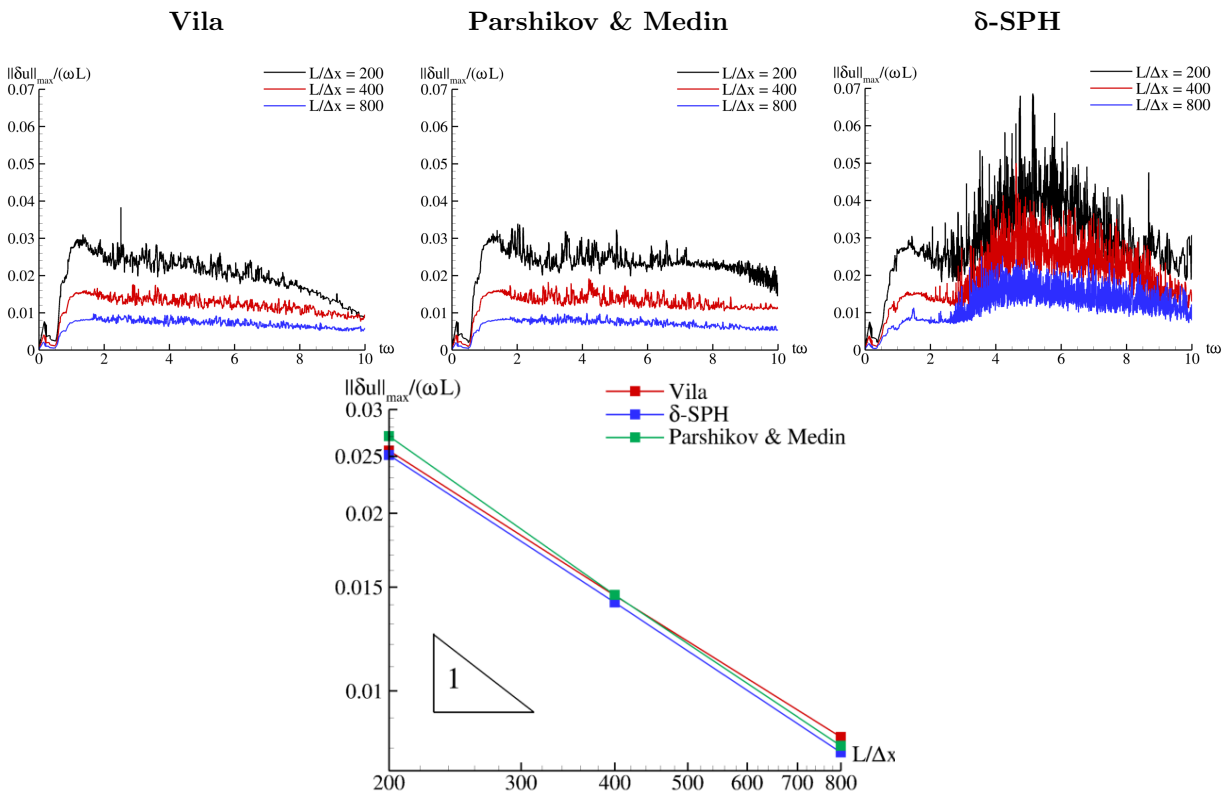

Figure 15: 2D rotating square patch. Top: time evolution of the maximum PST velocity $\|\boldsymbol{\delta u}\|_{max}$ for three spatial resolutions. Left: Vila scheme. Middle: Parshikov & Medin scheme. Right: δ-SPH scheme. Bottom: convergence rate of $\|\boldsymbol{\delta u}\|_{max}$ taken as the average in $t\omega \in [1.5; 2.5]$ for the three SPH schemes tested.

The time evolution of the maximum PST velocity is plotted in Fig. 15 for the three SPH schemes studied in this paper. By contrast with the stationary Taylor-Green case in Section 4, the maximum PST velocity $\|\boldsymbol{\delta u}\|_{max}$ decreases in the end of the simulation and this phenomenon is amplified for the coarse resolutions. This is due to the presence of thin jets appearing in this test case (see Fig. 16) where the PST is limited by the small values of λ_i. The two Riemann-based schemes give similar results in terms of $\|\boldsymbol{\delta u}\|_{max}$ whereas the signal is more noisy for the δ-SPH scheme. Nevertheless, the condition (9) is fulfilled for all the schemes with a convergence order close to the theoretical one (the convergence curve is obtained by averaging $\|\boldsymbol{\delta u}\|_{max}/(\omega L)$ between $t\omega = 1.5$ and $t\omega = 2.5$ to limit the influence of the noise on the convergence rate measure). For the finest spatial resolution $L/\Delta x = 800$, the maximum PST velocity is only about 1% of the maximum Lagrangian velocity in the fluid ($U^{max} = \omega L/\sqrt{2}$) and as we can see in Fig. 16, this is sufficient for breaking the anisotropic structures without affecting the pressure field.

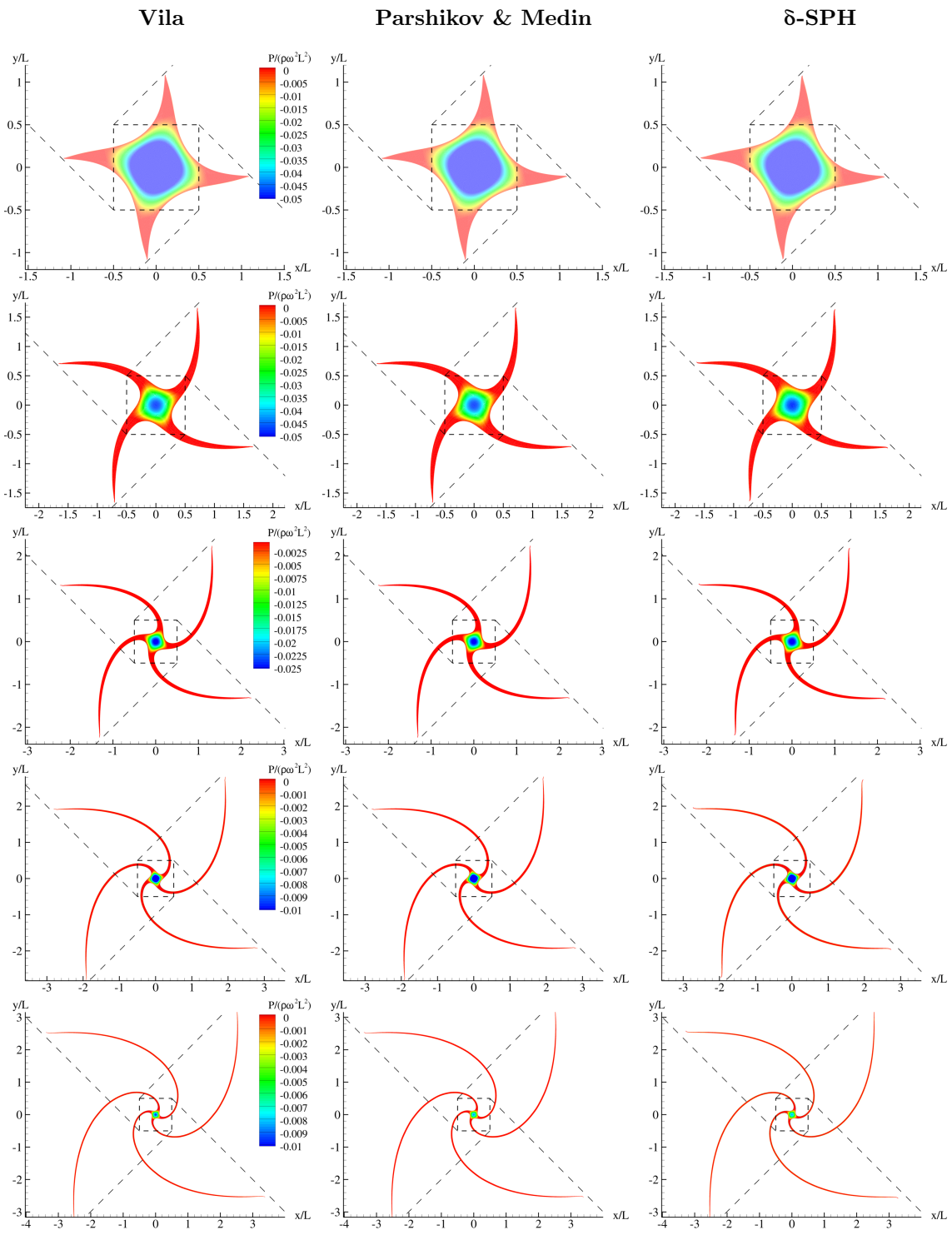

Figure 16: 2D rotating square patch. Pressure field obtained with $L/\Delta x = 800$ at $t\omega = 1.2,\ 2.4,\ 3.6,\ 4.8,\ 6.0$ (from top to bottom). Left: Vila scheme. Middle: Parshikov & Medin scheme. Right: δ-SPH scheme.

The time evolution of the pressure at the square center is plotted in the right part of Fig. 17 showing similar results with the three SPH schemes. Small oscillations are nevertheless observed with the ALE and

δ-SPH schemes. As already highlighted in [25] and [33], this phenomenon is due to the formulation and not to the PST itself. As a matter of fact, such oscillations do not occur using the Parshikov & Medin scheme, while the same level of PST velocity is reached. Furthermore, as shown in the left part of Fig. 17 where kinetic energy decay is plotted, the dissipation decreases as the spatial resolution increases. However, differences can be noted in comparison with Sun *et al.* [32], explained by the use of a higher nominal sound speed. A very similar kinetic energy decay is recovered while using $c_0 = 10U_{max}$ instead of $40U_{max}$ (see Fig. 18).

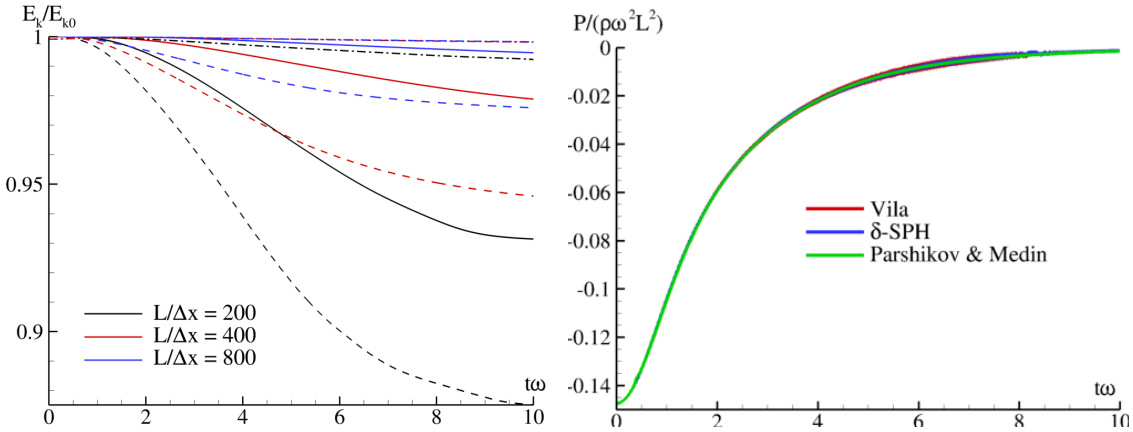

Figure 17: 2D rotating square patch. Left: kinetic energy decay obtained with three spatial resolutions. Solid: Vila scheme. Dot-dashed: Parshikov & Medin scheme. Dashed: δ-SPH scheme. Right: time evolution of the pressure at the center of the domain for the three SPH schemes tested with $L/\Delta x = 800$ and $c_0 = 40U_{max}$.

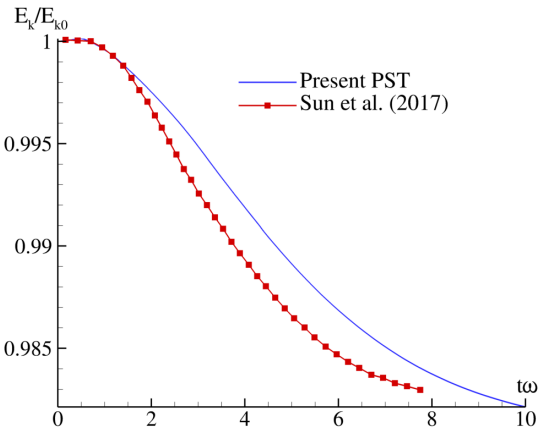

Figure 18: 2D rotating square patch. Kinetic energy decay using the δ-SPH scheme with $L/\Delta x = 400$ and $c_0 = 10U_{max}$, and comparison with the results obtained by Sun *et al.* [32].

6. PST in presence of free-surface and solid boundary: moving ghost particle method

In this section, the proposed PST is adapted in order to deal with solid boundaries using the volume-based method firstly developed in [16, 9]: the 'moving ghost particle' method. The validation is then performed for a jet impinging on a flat plate in 2D.

6.1. PST adaptation to ghost particles

Using the moving ghost particle method, ghost and fluid particles are considered indifferently in the PST computation for (i) the computation of $\widehat{\boldsymbol{\nabla}} C_i$ in Eq. (3), (ii) the free-surface detection, (iii) the determination of the normal vector to the free-surface. In order to theoretically recover the consistency property (15), the characteristic velocity U_i^{char} (and U_i^{lim}) has to be modified. Indeed, in order to respect the free-slip condition, the ghost particle velocity is mirrored:

$$\boldsymbol{u}_{\mathcal{G}_{i,s}} = \boldsymbol{u}_i - 2\left((\boldsymbol{u}_i - \boldsymbol{u}_s)\cdot\frac{\boldsymbol{x}_{\mathcal{G}_{i,s}} - \boldsymbol{x}_i}{\left\|\boldsymbol{x}_{\mathcal{G}_{i,s}} - \boldsymbol{x}_i\right\|}\right)\frac{\boldsymbol{x}_{\mathcal{G}_{i,s}} - \boldsymbol{x}_i}{\left\|\boldsymbol{x}_{\mathcal{G}_{i,s}} - \boldsymbol{x}_i\right\|}\ , \tag{49}$$

where $\boldsymbol{u}_s$ is the wall velocity at the normal projection s of particle i on the wall, $\boldsymbol{x}_{\mathcal{G}_{i,s}}$ and $\boldsymbol{u}_{\mathcal{G}_{i,s}}$ are the position and velocity of the ghost particle associated to the couple $i-s$ respectively. Then, we have:

$$\left|(\boldsymbol{u}_{\mathcal{G}_{i,s}} - \boldsymbol{u}_i)\cdot\frac{\boldsymbol{x}_{\mathcal{G}_{i,s}} - \boldsymbol{x}_i}{\left\|\boldsymbol{x}_{\mathcal{G}_{i,s}} - \boldsymbol{x}_i\right\|}\right| = 2\left|\boldsymbol{u}_i\cdot\frac{\boldsymbol{x}_{\mathcal{G}_{i,s}} - \boldsymbol{x}_i}{\left\|\boldsymbol{x}_{\mathcal{G}_{i,s}} - \boldsymbol{x}_i\right\|}\right| \underset{\Delta x\to 0}{\not\longrightarrow} 0\ , \tag{50}$$

since a fixed wall is considered here, i.e. $\boldsymbol{u}_s = \boldsymbol{0}$.

Consequently, the ghost particles are excluded from the computation of U_i^{char} and U_i^{lim} and the consistency property is recovered theoretically.

In presence of a triple point/line free-surface/solid boundary, the treatment exposed in Section 5.3 is applied.

6.2. Validation on a 2D jet impinging on a flat plate

In order to complete the validation of the PST introduced in this paper, the test case of a jet impinging on a flat plate is studied. The interest of this case relies on the presence of both a free-surface and a solid boundary. Furthermore, an analytical solution is available in 2D (see for instance [4]). This test case has also been studied using the SPH method in [12] [29] [10]. It consists in a jet of fluid of width H impacting a plate with an imposed velocity U. Then, the characteristic length, velocity, time and pressure are taken respectively as H, U, U/H and $\frac{\rho U^2}{2}$. The fluid impacts the plate with an angle $\alpha = 30°$ (see Fig. 19). An inlet condition is used to impose the jet velocity, while outlet conditions are prescribed at a distance taken as sufficiently far from the impact area (Fig. 19).

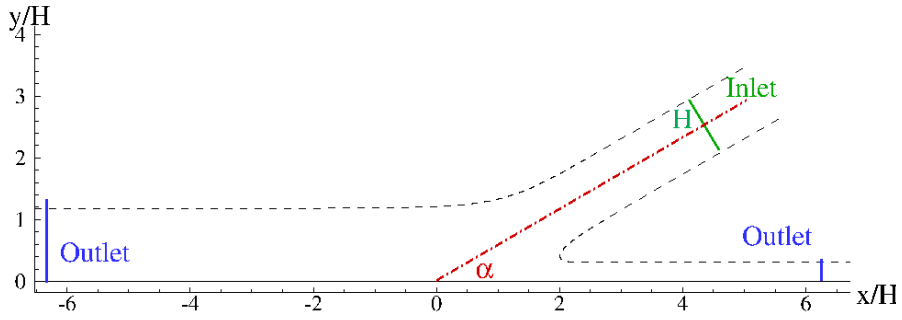

Figure 19: 2D jet impinging on a flat plate. Test case description.

In this section, the validation is performed in 2D and the sound speed is chosen as $c_0 = 11U$. As observed in Fig. 20 in which the maximum PST velocity is plotted, the consistency property is recovered for the three schemes studied. Using the δ-SPH scheme, $\|\boldsymbol{\delta u}\|_{max}$ is constant in time when the steady state is reached. Using the Vila scheme, we observe a sudden decrease of $\|\boldsymbol{\delta u}\|_{max}$ in the beginning of the simulation for the five spatial resolutions tested, and once the steady state reached $\|\boldsymbol{\delta u}\|_{max}$ is lower in average than in the two other schemes for the coarse resolutions. With the Parshikov & Medin scheme, $\|\boldsymbol{\delta u}\|_{max}$ is constant in

time when the steady state is reached for the coarse resolutions, and with $H/\Delta x = 120$ the results are close to those obtained with the Vila scheme. Despite these differences, the consistency property is recovered and the convergence rate is about 0.5 in this case.

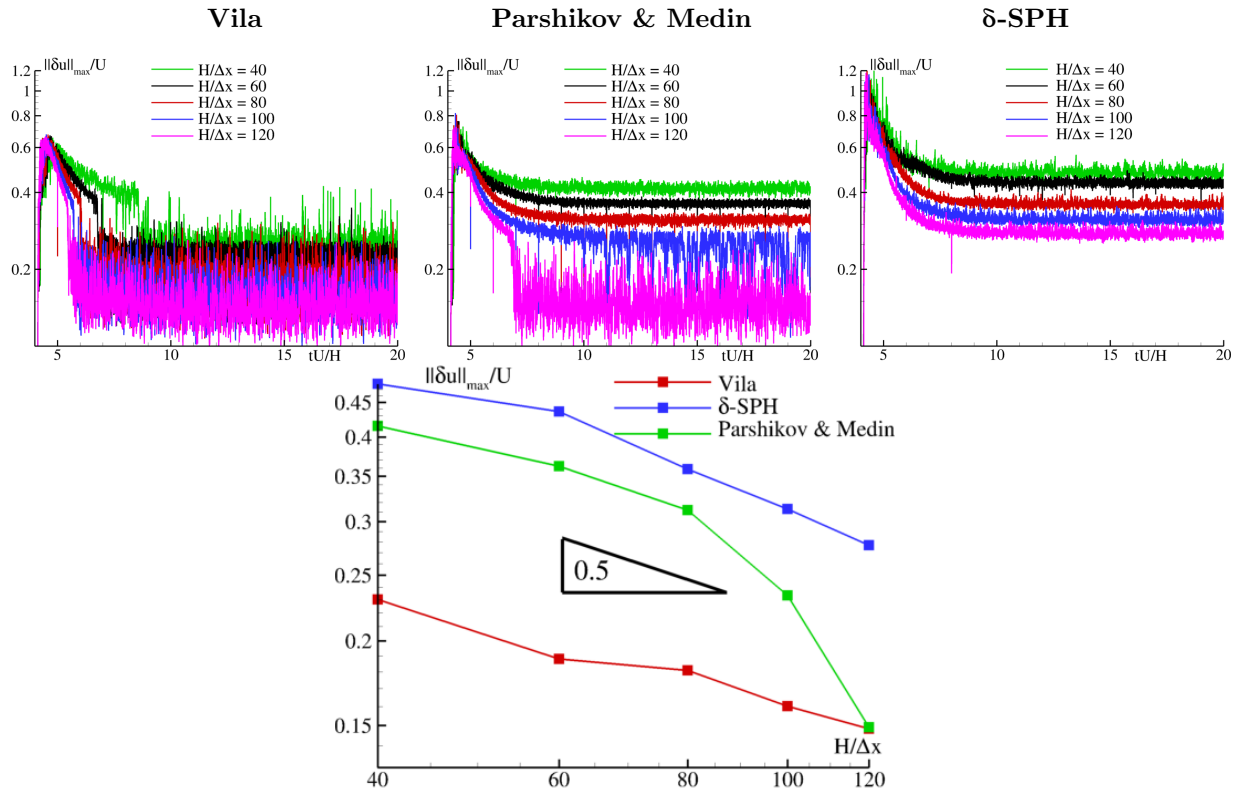

Figure 20: 2D jet impinging on a flat plate (ghost particle method). Top: time evolution of the maximum PST velocity $\|\boldsymbol{\delta u}\|_{max}$ for five spatial resolutions. Left: Vila scheme. Middle: Parshikov & Medin scheme. Right: δ-SPH scheme. Bottom: convergence rate of $\|\boldsymbol{\delta u}\|_{max}$ for the three SPH schemes tested.

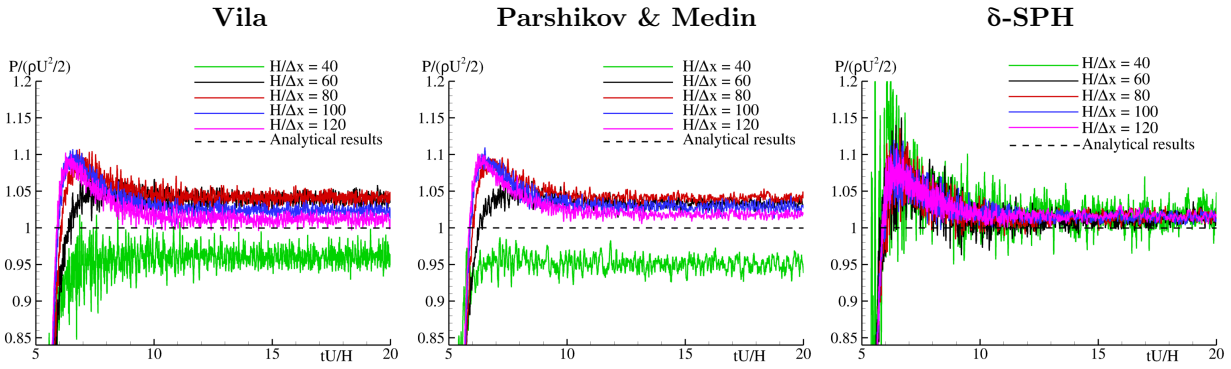

Figure 21: 2D jet impinging on a flat plate (ghost particle method). Time evolution of the pressure at the stagnation point for five spatial resolutions and comparison with the analytical results. Left: Vila scheme. Middle: Parshikov & Medin scheme. Right: δ-SPH scheme.

The time evolution of pressure at the stagnation point is plotted in Fig. 21. We can see that for the Riemann-based schemes, the analytical solution is almost obtained (less than 3% of error) with $H/\Delta x = 120$.

Using the δ-SPH scheme, the expected pressure is reached for a coarser spatial resolution, and refining the resolution allows for reducing the oscillations on the pressure signal. Finally, a good agreement is found in comparison to the analytical solution, as confirmed by the free-surface, pressure and velocity profiles shown in Fig. 22.

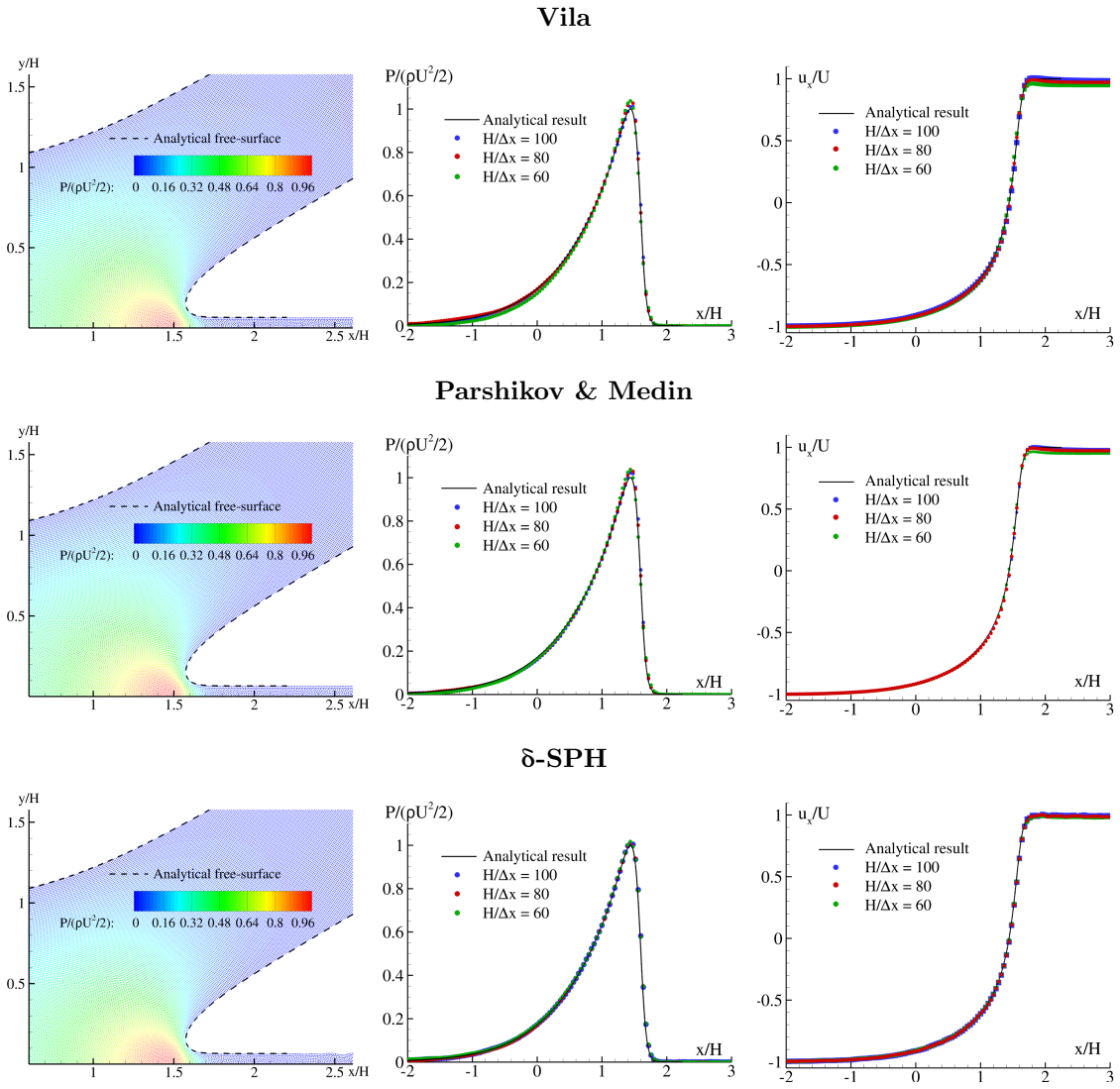

Figure 22: 2D jet impinging on a flat plate (ghost particle method). Solution obtained at $tU/H = 20$ and comparison with the analytical results with the Vila, Parshikov & Medin, and δ-SPH schemes (from top to bottom). Left: pressure field with $H/\Delta x = 100$ and comparison with the analytical free-surface. Center: pressure profile along the plate for three spatial resolutions. Right: velocity profile along the plate for three spatial resolutions.

7. PST in presence of free-surface and solid boundary: Boundary Integral Method

7.1. Adaptation of the PST

The solid boundary treatment used in this section is based on a Boundary Integral Method (BIM) and more especially the CutFace Approach (CFA) proposed by Chiron *et al.* [6]. Within this approach,

the intersection surface (noted $\partial\mathcal{D}_i$) between the kernel support of particle i and the solid boundary is discretized with a set of elements noted s. The SPH scheme obtained is briefly reminded in Eqs. (51)-(54):

$$\frac{d\boldsymbol{x}_i}{dt} = \boldsymbol{u}_{0i}, \tag{51}$$

$$\frac{dV_i}{dt} = \frac{V_i}{\gamma_i}\sum_{j\in\mathcal{D}_i} 2(\boldsymbol{u}_E-\boldsymbol{u}_i).\boldsymbol{\nabla}_i W_{ij}V_j + \frac{V_i}{\gamma_i}\sum_{s\in\partial\mathcal{D}_i}(\boldsymbol{u}_s-\boldsymbol{u}_i).\boldsymbol{n}_s W_{is}S_s, \tag{52}$$

$$\frac{d\left(V_i\rho_i\right)}{dt} = 0, \tag{53}$$

$$\frac{d\left(V_i\rho_i\boldsymbol{u}_i\right)}{dt} = -\frac{V_i}{\gamma_i}\sum_{j\in\mathcal{D}_i} 2P_E\boldsymbol{\nabla}_i W_{ij}V_j - \frac{V_i}{\gamma_i}\sum_{s\in\partial\mathcal{D}_i}(P_s+P_i)W_{is}\boldsymbol{n}_s S_s + V_i\rho_i\boldsymbol{g}, \tag{54}$$

where $\boldsymbol{n}_s$, S_s, γ_i, $\boldsymbol{u}_s$ and P_s are respectively the normal vector to s, the surface value of s, the renormalization factor, the velocity of the solid boundary at the center of s and the pressure value on s.

Therefore, in presence of such a surface-based method for the solid boundary treatment, an adaptation regarding the PST has to be carried out. Firstly, in the free-surface detection algorithm, the surface terms have to be taken into account within the computation of the minimum eigenvalues λ_i in order to distinguish the particles close to a solid boundary from the particles close to a free-surface. To this end, the modified renormalization matrix defined in Eq. (55) is used (as introduced in [5]).

$$\mathbb{L}_i^{BIM-CFA} = \left(\frac{1}{\gamma_i}\sum_{j\in\mathcal{D}_i}(\boldsymbol{x}_j-\boldsymbol{x}_i)\otimes\boldsymbol{\nabla}_i W_{ij}V_j + \frac{1}{\gamma_i}\sum_{s\in\partial\mathcal{D}_i}(\boldsymbol{x}_s-\boldsymbol{x}_i)\otimes\boldsymbol{n}_s W_{is}S_s\right)^{-1}. \tag{55}$$

Secondly, using Eq. (3) close to a boundary results in a vector always pointing outwards the fluid. To recover a vector pointing towards the zones of low concentration of particles, the boundary has to be taken into account within the approximation of $\widehat{\boldsymbol{\nabla}}C$. This is achieved through Eq. (56), as:

$$\widehat{\boldsymbol{\nabla}}C_i^{BIM-CFA} = \sum_{j\in\mathcal{D}_i}\left[1+0.2\left(\frac{W_{ij}}{W(\Delta x_i)}\right)^4\right]\boldsymbol{\nabla}_i W_{ij}V_j + \sum_{s\in\partial\mathcal{D}_i}\left[1+0.2\left(\frac{W_{is}}{W(\Delta x_i)}\right)^4\right]\boldsymbol{n}_s W_{is}S_s\ . \tag{56}$$

Finally, the normal vector to the free-surface is computed as:

$$\boldsymbol{n}_i^{BIM-CFA} = -\frac{\mathbb{L}_i^{BIM-CFA}\boldsymbol{\nabla}C_i^{BIM-CFA}}{\left\|\mathbb{L}_i^{BIM-CFA}\boldsymbol{\nabla}C_i^{BIM-CFA}\right\|}\ ,\ \text{where}\ \boldsymbol{\nabla}C_i^{BIM-CFA} = \sum_{j\in\mathcal{D}_i}\boldsymbol{\nabla}_i W_{ij}V_j + \sum_{s\in\partial\mathcal{D}_i}\boldsymbol{n}_s W_{is}S_s\ . \tag{57}$$

Like with the moving ghost particle method, the terms $\boldsymbol{u}_i-\boldsymbol{u}_s$ (in which the velocity of the solid boundary appears) are excluded from the computation of U_i^{char} and U_i^{lim}. Indeed, during an impact of fluid on a solid boundary for instance, at the instant just before the impact, the relative velocity reads (here a fixed boundary is considered: $\boldsymbol{u}_s=\boldsymbol{0}$):

$$\boldsymbol{u}_i-\boldsymbol{u}_s = \boldsymbol{u}_i \underset{\Delta x\to 0}{\not\longrightarrow} \boldsymbol{0}\ , \tag{58}$$

and taking these terms into account would lead to: $\lim\limits_{\Delta x\to 0} U_i^{char} \neq 0$.

In a first attempt, this boundary treatment has been implemented only within the Riemann-based formulation for which the PST is taken into account in the motion equation only (Parshikov & Medin scheme). Therefore, the validation of the proposed PST in presence of a solid boundary modelled by the boundary-integral method is performed exclusively using this scheme in the following. Note that the modifications brought do not affect both the Galilean and local rotation invariance, and the independence of the PST from the solution.

7.2. Tangential PST to solid boundary

In a similar way as for the free-surface, a kinematic condition has to be fulfilled at a solid boundary, which reads $\boldsymbol{u}_f.\boldsymbol{n}_s = \boldsymbol{u}_s.\boldsymbol{n}_s$ in case of a free-slip condition, where $\boldsymbol{u}_f$ and $\boldsymbol{u}_s$ stand for the fluid and solid boundary velocity respectively and $\boldsymbol{n}_s$ is the normal to the solid boundary. Consequently, in order to ensure this condition, the normal component of the PST velocity should be deleted close to solid boundaries modelled by boundary integrals (as proposed in [34] for example). Nevertheless, limiting the PST to its tangential component can lead in practice to undesired effects, as shown in the right plot of Fig. 23, where the normal component of the PST is canceled, leading to an anisotropic particle clustering along the boundary. This wrong effect is absent when not limiting the shifting direction close to a solid boundary (as visible in the left plot of Fig. 23), which sounds therefore as preferable. In addition, this short distance between the particles and a solid boundary implies a wrong estimation of the pressure in near boundary areas. Fig. 24 illustrates this effect, as using a purely tangential PST produces an overestimation of the pressure along the plate, whereas analytical results are recovered otherwise.

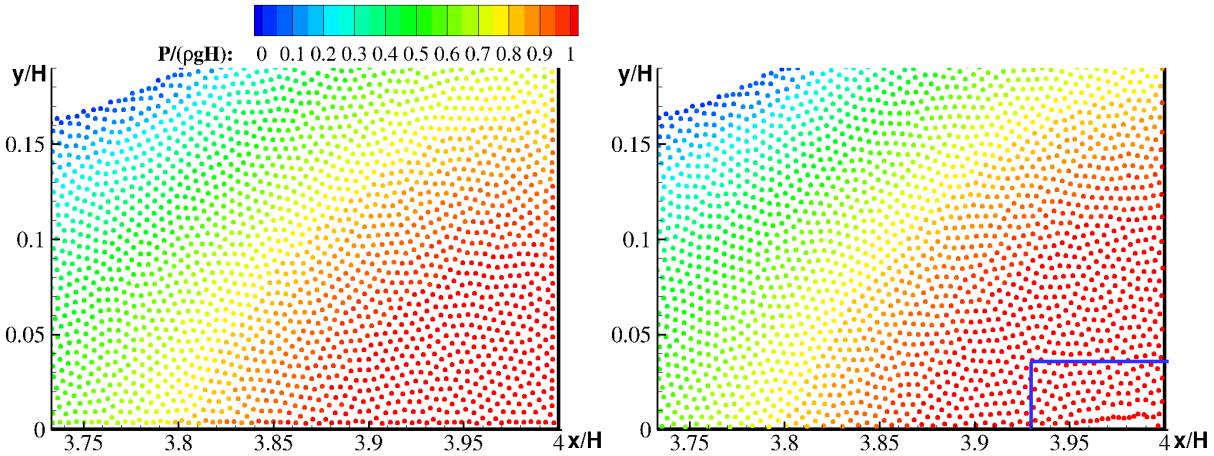

Figure 23: Example of particle distributions obtained without (left) or with (right) limitation of the PST velocity to its tangential component (Parshikov & Medin scheme with BIM-CFA). Case of a dam-break after impacting the opposite wall.

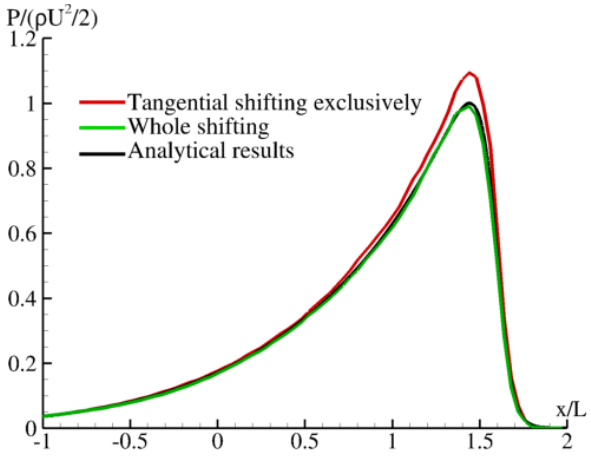

Figure 24: 2D jet impinging on a flat plate (Parshikov & Medin scheme with BIM-CFA). Pressure along the plate at $tU/H = 0.2$ with $H/\Delta x = 80$.

7.3. Validation of the PST in presence of free-surface and solid boundaries in 2D and 3D

7.3.1. Validation: 2D impinging jet on a flat plate

The use of a boundary integral method is responsible for an additional term in Eq. (56), so that it is needed to check whether the property (9) is still respected in that case. This is actually confirmed in Fig. 25, which shows that the maximum PST velocity $\|\boldsymbol{\delta u}\|_{max}$ goes towards zero as the spatial resolution increases, and the convergence rate is about 0.5 (measured once the steady state has been reached). Note that the differences observed between the surface and volume based boundary methods for the finest spatial resolution depend on the choice of the norm, L^2 here. Indeed, similar results are found for both boundary methods when using the L^∞ norm to compute the convergence rate.

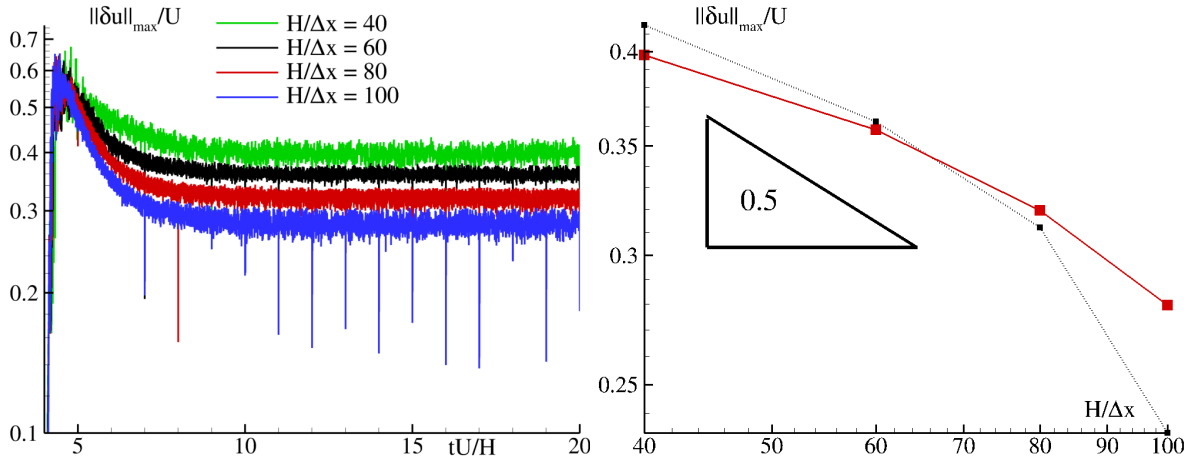

Figure 25: 2D jet impinging on a flat plate. Left: time evolution of the maximum PST velocity $\|\boldsymbol{\delta u}\|_{max}$ for four spatial resolutions (Parshikov & Medin scheme with BIM-CFA). Right: in red, convergence rate of $\|\boldsymbol{\delta u}\|_{max}$ for the Parshikov & Medin scheme with the BIM-CFA method (the results with the Parshikov & Medin scheme with the moving ghost particles method are recalled in black dotted for comparison purpose).

The left part of Fig. 26 shows the time history of pressure at the stagnation point, for which a correct capture of the pressure peak is obtained, provided that a fine enough spatial resolution is used ($H/\Delta x = 80$). Note that using the surface-based method allows for recovering the analytical results with a coarser spatial resolution than with the volume-based method (see comparison with Figs. 21 and 22). Furthermore, the pressure profile along the plate is in good agreement with the analytical results, as visible in the right plot of Fig. 26.

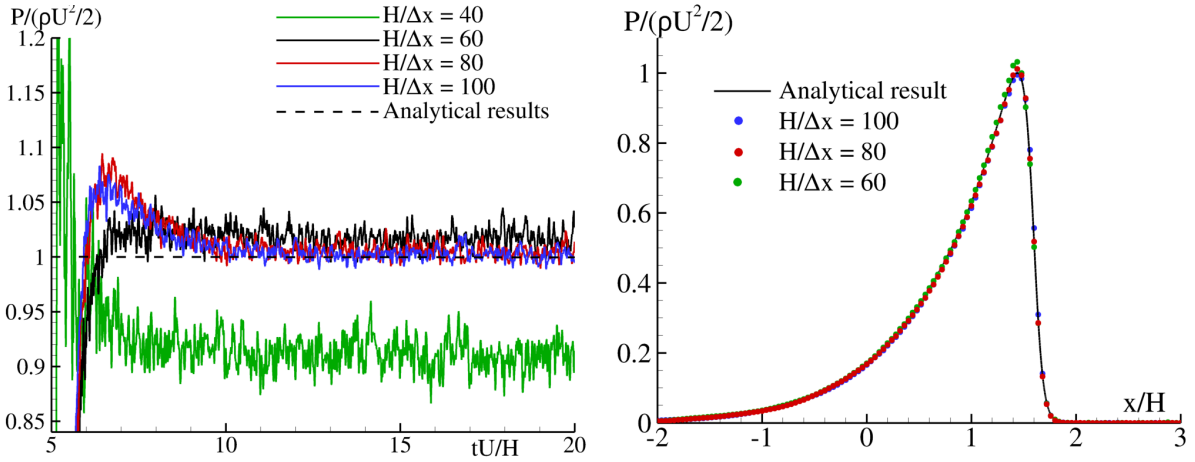

Figure 26: 2D jet impinging on a flat plate (Parshikov & Medin scheme with BIM-CFA). Left: time evolution of the pressure at the stagnation point for four spatial resolutions and comparison to the analytical solution. Right: pressure profile along the plate for different spatial resolutions and comparison to the analytical solution once the steady state reached (at $tU/H = 20$).

The left plot of Fig. 27 displays the SPH pressure field solution obtained, and the analytical free-surface is also plotted, showing a good agreement. Moreover, the velocity profile along the plate converges towards the analytical solution while refining the spatial resolution, as shown in the right plot of Fig. 27.

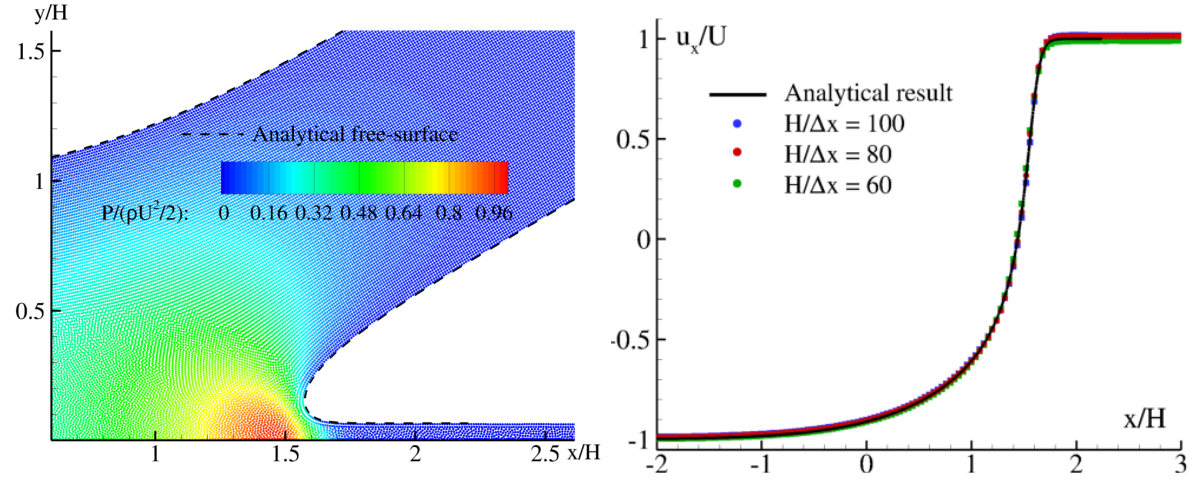

Figure 27: 2D jet impinging on a flat plate (Parshikov & Medin scheme with BIM-CFA). Left: pressure field with $H/\Delta x = 100$ at $tU/H = 20$ (the analytical free-surface is also plotted). Right: velocity profile along the plate for different spatial resolutions compared to the analytical solution.

7.3.2. Validation: 3D impinging jet on a flat plate

The impinging jet on a flat plate in 3D is studied in this work with the angle $\alpha = 90°$ (see Fig. 19). The reference solution is taken here as the experimental results obtained in [13] in which pressure profiles along the plate and the free-surface shape are provided. The Froude number ($Fr \approx 36$) involved in the experimentation allows for neglecting the gravity effect. Furthermore, the Reynolds number ($Re \approx 6.10^5$) is such that viscous effects can also be neglected in a first attempt. Then, applying the Bernoulli's equation along the central flow streamline provides the expected pressure at the stagnation point. Fig. 28 shows that the property (9) is still verified in that 3D case and the first order of convergence is retrieved. Furthermore,

as observed in Fig. 29, the pressure peak converges towards the analytical result while refining the spatial resolution, although a converged result is not reached yet with $H/\Delta x = 40$. Regarding the pressure profile along the plate at different locations (see Fig. 30), the results obtained with the discretization $H/\Delta x = 40$ are close to those measured in [13], but an underestimation of the pressure is still found, especially at $y/H = 0.53$. This is also observed numerically by Kvicinsky [13] with the CFD code FIDAP based on the Finite Element method (Galerkin method). In our case, this pressure underestimation shall be explained by the spatial resolution used. Actually, since the pressure result is not yet converged at the stagnation point it is, logically, not the case either elsewhere along the plate. Note also that a spurious asymmetry is observed in the experiment but, logically, not in the numerical results. Finally, Fig. 31 presents views of the numerical solution, together with a comparison with the experimental free-surface provided by Kvicinsky [13], showing a good agreement. Furthermore, we can observe a good particle distribution (considering that the right plot is a 2D slice of a 3D computation), providing a regular pressure field despite the coarse resolution used.

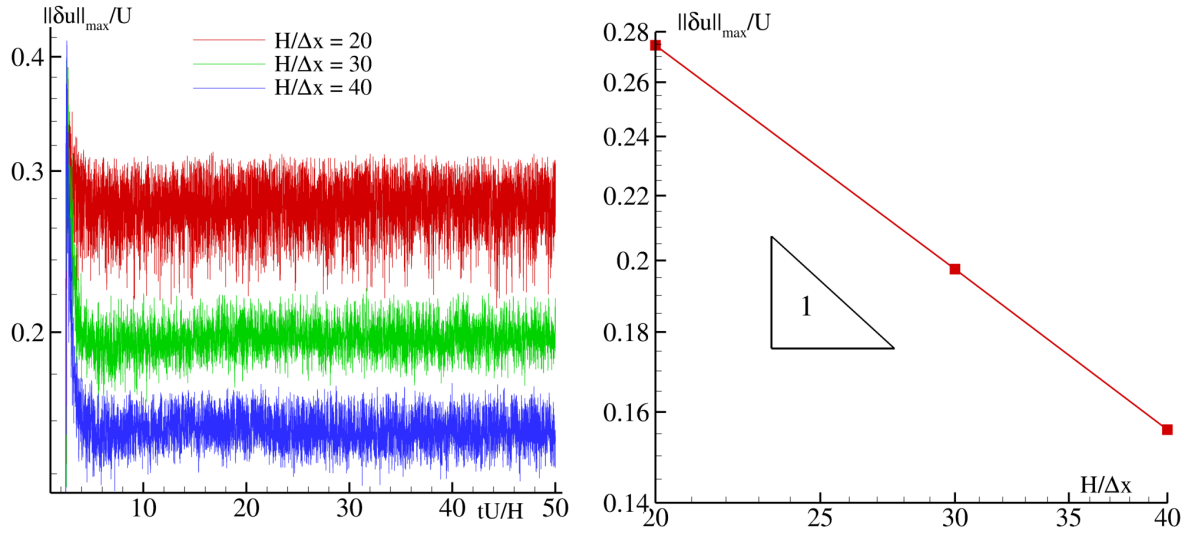

Figure 28: 3D impinging jet on a flat plate (Parshikov & Medin scheme with BIM-CFA). Left: time evolution of the maximum PST velocity for three spatial resolutions. Right: Convergence rate of the maximum PST velocity.

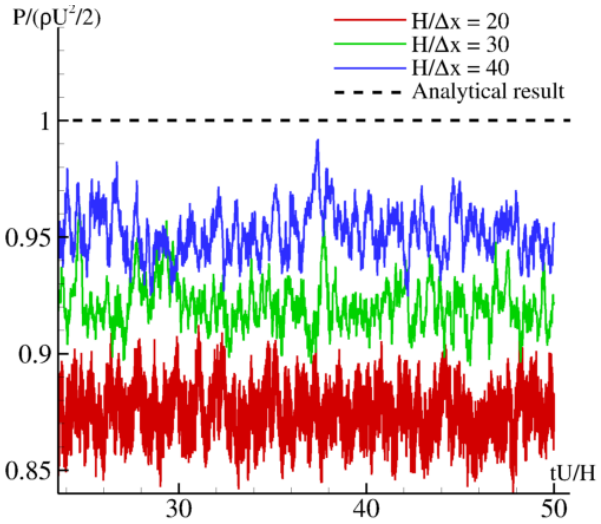

Figure 29: 3D impinging jet on a flat plate (Parshikov & Medin scheme with BIM-CFA). Time evolution of the pressure at the stagnation point location for three spatial resolutions and comparison with the analytical result.

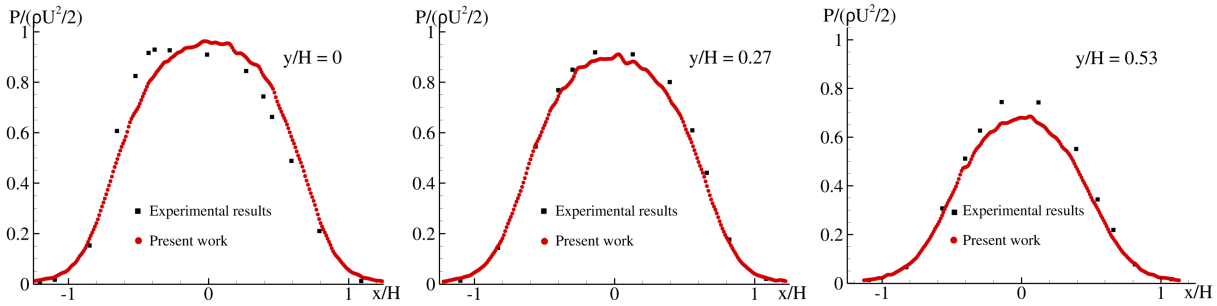

Figure 30: 3D impinging jet on a flat plate (Parshikov & Medin scheme with BIM-CFA). Pressure profile along the plate at $tU/H = 50$ at different locations y ($y/H = 0$, $y/H = 0.27$ and $y/H = 0.53$ from left to right) with the spatial resolution $H/\Delta x = 40$ and comparison with the experimental result of Kvicinsky [13].

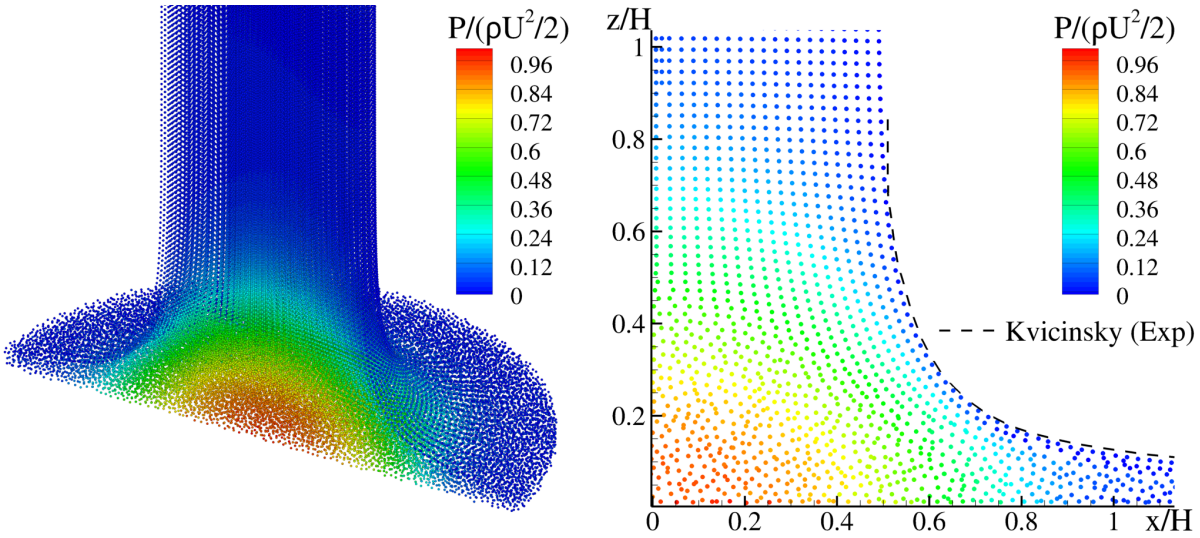

Figure 31: 3D impinging jet on a flat plate (Parshikov & Medin scheme with BIM-CFA). Results obtained at $tU/H = 50$ with $H/\Delta x = 40$. Left: global view with pressure contour. Right: slice of the flow and comparison with the experimental free-surface.

8. Conclusion

In this paper, Particle Shifting Techniques introduced in the SPH literature have been briefly recalled and analyzed and a specific attention has been paid to those based on Fick's law which allows for the particles to slightly move from zones of high concentration to zones of low concentration. Then, conditions that should be verified by a PST (consistency of the PST velocity, Galilean and local rotation invariance, independence between local PST and global fluid flow) have been exposed. Using a theoretical demonstration in one dimension, it has been shown that using a PST based on Fick's law together with a characteristic velocity based on the Lagrangian velocity of the flow (local or global), as done in the literature, does not ensure the respect of such conditions. In order to recover theoretically these three conditions, using a relative velocity instead of the Lagrangian one is sufficient and a novel PST has been then derived and validated on different test cases. It has especially been shown on a Taylor-Green vortex test case that this new PST is actually consistent in practice contrary to existing PSTs of the literature, and yields more accurate results.

A theoretical convergence development of SPH gradients close to a free-surface in presence of particle disorder has then been derived so as to extend the proposed PST to the presence of a free-surface, still verifying these three theoretical conditions. Finally, the extension of the proposed PST to the presence of a solid boundary in addition to a free-surface has been performed, both for volume-based (ghost particle) and surface-based (boundary integral method) SPH boundary treatments, again with targeting the fulfillment of the three formulated theoretical conditions.

The PST introduced in this paper is not linked to a specific SPH scheme and therefore the validation of its fulfillment of the three formulated theoretical conditions is performed with three different SPH schemes, all based on the weakly-compressible assumption. These theoretical conditions have then been actually verified numerically for these three schemes, in 2D respectively for an infinite domain (Taylor-Green vortices), in the presence of a free-surface (rotating square patch) and with both free-surface and solid boundary modelled by the moving ghost particle method (impinging jet on a flat plate) with convergence rates of the PST velocity between 0.5 and 1 and good agreement with the reference solutions. Finally, the PST has been adapted to a boundary integral method to model boundaries and validated in 2D and 3D, showing that the three formulated theoretical conditions were still numerically verified and a good accuracy obtained in comparison with reference solutions.

Moreover, this novel PST has the advantage of being independent of the nominal sound speed, contrary to some PST proposed in the literature, providing it a natural compatibility (a priori) with the incompressible assumption.

Appendix

The aim of this appendix is to detail the extension of the result (10) in presence of a free-surface. In 1D, a free-surface is characterized by a semi-infinite domain (e.g., if the particle i is located at the free-surface $x = x_i$, then the fluid domain can be considered as $[x_i, +\infty[$). In addition, we consider here that the particles are not distributed uniformly within the kernel support. To this end, the particles j are assumed to be located at $\bar{x}_j$ positions that are generally different from the positions x_j that they would have occupied in a uniform distribution (as illustrated in Fig. 32) and the volume associated to a particle j is noted Δx_j (a priori different from Δx).

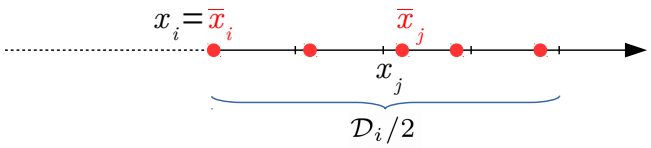

Figure 32: Parameters used for the theoretical study at the free-surface.

The first step consists in decomposing the continuous expression of the SPH gradient operator on the intervals $\left[\bar{x}_j - \frac{\Delta x_j}{2}, \bar{x}_j + \frac{\Delta x_j}{2}\right]$ (note that, in 1D, the gradient is equivalent to a first order spatial derivative), and using a Taylor expansion on the terms under the integral, which leads to:

$$\begin{aligned}\int_{x_i}^{x_i+R} AW'dx &= \sum_{j\in\mathcal{D}_i/2} \int_{\bar{x}_j-\frac{\Delta x_j}{2}}^{\bar{x}_j+\frac{\Delta x_j}{2}} AW'dx \\ &= \sum_{j\in\mathcal{D}_i/2} \int_{\bar{x}_j-\frac{\Delta x_j}{2}}^{\bar{x}_j+\frac{\Delta x_j}{2}} \left[A_i + (x-x_i)\,A_i' + ...\right]\left[W'j + (x-x_j)\,W_j'' + ...\right] dx,\end{aligned} \tag{59}$$

where $\mathcal{D}_i/2$ stands for the half-filled kernel support. Following the idea of Quinlan *et al.* [27], the change of variables:

$$\hat{W}_i(s) = RW\left(x - x_i\right), \quad s = \frac{x - x_i}{R}, \quad s_j = \frac{x_j - x_i}{R}, \tag{60}$$

is performed on the right hand side of Eq. (59), implying that $s \in [0;1]$ and that the quantity $\hat{W}$ is $O(1)$ (as well as all its successive spatial derivatives). We also define the values $\Delta s_j = \frac{\Delta x_j}{R}$ and $\bar{s}_j = \frac{\bar{x}_j - x_i}{R}$, corresponding respectively to the dimensionless volume and position of the particle j. As made in [27], the term $A_i W_j'$ can be approximated by $A_i W_j' \simeq A_j W_j'$ (see [27] for more details). Then expression (59) becomes:

$$\begin{aligned}\int_{x_i}^{x_i+R} AW'dx = &\sum_{j\in\mathcal{D}_i/2} A_j W'_j \Delta x_j + \sum_{j\in\mathcal{D}_i/2} \left(A'_i \hat{W}'_j + \frac{1}{R} A_i \hat{W}''_j\right) \int (s-s_j)\, ds \\ &+ \sum_{j\in\mathcal{D}_i/2} \frac{1}{2R} A_i \hat{W}'''_j \int (s-s_j)^2\, ds + \sum_{j\in\mathcal{D}_i/2} A'_i \hat{W}''_j \int s\,(s-s_j)\, ds \\ &+ \sum_{j\in\mathcal{D}_i/2} \frac{R}{2} A''_i \hat{W}'_j \left(\int s^2 ds - s_j^2 \int ds\right) + ...,\end{aligned} \tag{61}$$

where the integrals on the right hand side are evaluated on the interval $\left[\bar{s}_j - \frac{\Delta s_j}{2}, \bar{s}_j + \frac{\Delta s_j}{2}\right]$. We then define the variable $\xi_j = \frac{\bar{x}_j - x_j}{\Delta x_j}$, which can be interpreted as a measure of the local particle disorder (if $\xi_j = 0$ then particles are located on a regular lattice; on the contrary, the more ξ_j differs from 0 the more disordered is the particles distribution). Calculating the integrals in the expression (61) leads after algebra to:

$$\begin{aligned}\sum_{j\in\mathcal{D}_i/2} A_j W'_j \Delta x_j - \int_{x_i}^{x_i+R} AW'dx = &-A'_i \sum_{j\in\mathcal{D}_i/2} \hat{W}'_j \xi_j \Delta s_j^2 - \frac{A_i}{R} \sum_{j\in\mathcal{D}_i/2} \hat{W}''_j \xi_j \Delta s_j^2 \\ &- \frac{A_i}{2R} \sum_{j\in\mathcal{D}_i/2} \hat{W}'''_j \left(\frac{\Delta s_j^2}{12} + \xi_j^2 \Delta s_j^2\right) \Delta s_j \\ &- A'_i \sum_{j\in\mathcal{D}_i/2} \hat{W}''_j \left(\frac{\Delta s_j^2}{12} + \bar{s}_j \xi_j \Delta s_j\right) \Delta s_j \\ &- A''_i \frac{R}{2} \sum_{j\in\mathcal{D}_i/2} \hat{W}'_j \left(\frac{\Delta s_j^2}{12} + (\bar{s}_j + s_j)\, \xi_j \Delta s_j\right) \Delta s_j + ...\end{aligned} \tag{62}$$

The exact values of the different sums on the right hand side are difficult to evaluate, as they depend on the exact positions $\bar{x}_j$ of particles j which are unknown a priori. In order to estimate these different sums, the terms ξ_j and Δs_j are replaced by their mean values ξ and $\Delta s = \frac{\Delta x}{R}$ and moved outside the summations, one term Δs_j being retained inside each sum in order to approximate the sums by integrals. Then the following approximations can be made:

$$\sum_{j\in\mathcal{D}_i/2} \hat{W}'_j \xi_j \Delta s_j^2 \simeq \delta\Delta s \sum_{j\in\mathcal{D}_i/2} \hat{W}'_j \Delta s_j \simeq \xi\Delta s \int_0^1 \hat{W}' ds \tag{63}$$

$$\sum_{j\in\mathcal{D}_i/2} \hat{W}''_j \xi_j \Delta s_j^2 \simeq \delta\Delta s \sum_{j\in\mathcal{D}_i/2} \hat{W}''_j \Delta s_j \simeq \xi\Delta s \int_0^1 \hat{W}'' ds \tag{64}$$

$$\sum_{j\in\mathcal{D}_i/2} \hat{W}'''_j \Delta s_j^3 \simeq \Delta s^2 \sum_{j\in\mathcal{D}_i/2} \hat{W}'''_j \Delta s_j \simeq \Delta s^2 \int_0^1 \hat{W}''' ds \tag{65}$$

$$\sum_{j\in\mathcal{D}_i/2} \hat{W}'''_j \xi_j^2 \Delta s_j^3 \simeq \xi^2\Delta s^2 \sum_{j\in\mathcal{D}_i/2} \hat{W}'''_j \Delta s_j \simeq \xi^2\Delta s^2 \int_0^1 \hat{W}''' ds \tag{66}$$

$$\sum_{j\in\mathcal{D}_i/2} \hat{W}''_j \Delta s_j^3 \simeq \Delta s^2 \sum_{j\in\mathcal{D}_i/2} \hat{W}''_j \Delta s_j \simeq \Delta s^2 \int_0^1 \hat{W}'' ds \tag{67}$$

$$\sum_{j\in\mathcal{D}_i/2} \hat{W}''_j \bar{s}_j \xi_j \Delta s_j^2 \simeq \xi\Delta s \sum_{j\in\mathcal{D}_i/2} \bar{s}_j \hat{W}''_j \Delta s_j \simeq \xi\Delta s \int_0^1 s\hat{W}'' ds \tag{68}$$

$$\sum_{j\in\mathcal{D}_i/2} \hat{W}'_j \Delta s_j^3 \simeq \Delta s^2 \sum_{j\in\mathcal{D}_i/2} \hat{W}'_j \Delta s_j \simeq \Delta s^2 \int_0^1 \hat{W}' ds \tag{69}$$

$$\sum_{j\in\mathcal{D}_i/2} \hat{W}'_j \left(\bar{s}_j + s_j\right) \xi_j \Delta s_j^2 \simeq \xi\Delta s \sum_{j\in\mathcal{D}_i/2} \hat{W}'_j \left(\bar{s}_j + s_j\right) \Delta s_j \simeq \xi\Delta s \int_0^1 2s\hat{W}' ds. \tag{70}$$

The change of variables (60) implies that all the integrals in the previous expression are $O(1)$ (in particular we can notice that the half-filled kernel support implies that all these integrals are a priori different from zero, despite the kernel function is still symmetrical). The only remaining term to evaluate is the integral $\int_{x_i}^{x_i+R} AW'dx$. To this end, a simple integration by parts is used here leading to:

$$\int_{x_i}^{x_i+R} AW'dx = \left[AW\right]_{x_i}^{x_i+R} - \int_{x_i}^{x_i+R} A'Wdx = -A_iW_i - \int_{x_i}^{x_i+R} A'Wdx. \tag{71}$$

And the change of variables shows that $A_iW_i = \frac{A_i}{R}O(1)$ (the other term is at a higher order). Then expression (62) can be expressed in terms of orders of magnitude. Finally the truncation error for a half-filled kernel support (e.g., in presence of a free-surface) is given by:

$$\begin{aligned}\sum_{j\in\mathcal{D}_i/2} A_j \boldsymbol{\nabla} W_{ij} V_j - A'_i = \frac{A_i}{R}\left[O(1) + \xi O\left(\frac{\Delta x}{R}\right) + \frac{1}{2}\left(\xi^2 + \frac{1}{12}\right) O\left(\left(\frac{\Delta x}{R}\right)^2\right)\right] \\ + A'_i\left[O(1) + \xi O\left(\frac{\Delta x}{R}\right) + O\left(\left(\frac{\Delta x}{R}\right)^2\right)\right] \\ + A''_i R\left[\xi O\left(\frac{\Delta x}{R}\right) + O\left(\left(\frac{\Delta x}{R}\right)^2\right)\right] + ...\end{aligned} \tag{72}$$

References

References

[1] S. Adami, X.Y. Hu, and N.A. Adams. A transport-velocity formulation for smoothed particle hydrodynamics. *Journal of Computational Physics*, 241:292–307, 2013.

[2] M. Antuono, B. Bouscasse, A. Colagrossi, and S. Marrone. A measure of spatial disorder in particle methods. *Computer Physics Communications*, 185:2609–2621, 2014.
[3] M. Antuono, A. Colagrossi, S. Marrone, and C. Lugni. Propagation of gravity waves through an SPH scheme with numerical diffusive terms. *Computer Physics Communications*, 182(4):866–877, 2011.
[4] M. Antuono, A. Colagrossi, S. Marrone, and D. Molteni. Free-surface flows solved by means of SPH schemes with numerical diffusive terms. *Computer Physics Communications*, 181(3):532–549, 2010.
[5] L. Chiron. *Coupling and improvements of the SPH method to treat flows involving temporal and spatial multi-scales*. PhD thesis, Ecole Centrale de Nantes (ECN), March 2017.
[6] L. Chiron, M. De Leffe, G. Oger, and D. Le Touzé. Fast and accurate SPH modelling of 3D complex wall boundaries in viscous and non viscous flows. *Computer Physics Communications*, 234:93–111, 2019.
[7] A. Colagrossi, M. Antuono, S. Marrone, P.N. Sun, and A.M. Zhang. Notes on the SPH model within the Arbitrary-Lagrangian-Eulerian framework. In *13th international SPHERIC workshop*, pages 22–29, 2018.
[8] A. Colagrossi, B. Bouscasse, M. Antuono, and S. Marrone. Particle packing algorithm for SPH schemes. *Computer Physics Communications*, 183(2):1641–1683, 2012.
[9] A. Colagrossi and M. Landrini. Numerical simulation of interfacial flows by smoothed particle hydrodynamics. *Journal of Computational Physics*, 191(2):448 – 475, 2003.
[10] M.D. Green, R. Vacondio, and J. Peiró. A smoothed particle hydrodynamics numerical scheme with a consistent diffusion term for the continuity equation. *Computers & Fluids*, 179:632 – 644, 2019.
[11] A. Khayyer, H. Gotoh, and Y. Shimizu. Comparative study on accuracy and conservation properties of two particle regularization schemes and proposal of an optimized particle shifting scheme in ISPH context. *Journal of Computational Physics*, 332:236 – 256, 2017.
[12] P.K. Koukouvinis, J.S. Anagnostopoulos, and D.E. Papantonis. An improved MUSCL treatment for the SPH-ALE method: comparison with the standard SPH method for the jet impingement case. *International Journal for Numerical Methods in Fluids*, 71(9):1152–1177, 2013.
[13] S. Kvicinsky. *Méthode d'analyse des écoulements 3D à surface libre : application aux turbines Pelton*. PhD thesis, École Polytechnique Fédérale de Lausanne (EPFL), 2002.
[14] D. Le Touzé, A. Colagrossi, G. Colicchio, and M. Greco. A critical investigation of smoothed particle hydrodynamics applied to problems with free-surfaces. *International Journal for Numerical Methods in Fluids*, 73(7):660 – 691, 2013.
[15] J. Leduc, F. Leboeuf, M. Lance, E. Parkinson, and J.-C. Marongiu. Improvement of multiphase model using preconditioned Riemann solvers. In *Proceedings of the* 5^{th} *international SPHERIC workshop*, pages 1–6, 2010.
[16] L.D. Libersky, A.G. Petschek, T.C. Carney, J.R. Hipp, and F.A. Allahdadi. High strain Lagrangian hydrodynamics a three-dimensional SPH code for dynamic material response. *Journal of Computational Physics*, 109(1):67–75, 1993.
[17] S.J. Lind, R. Xu, P.K. Stansby, and B.D. Rogers. Incompressible smoothed particle hydrodynamics for free-surface flows: A generalised diffusion-based algorithm for stability and validations for impulsive flows and propagating waves. *Journal of Computational Physics*, 231(4):1499–1523, 2012.
[18] S. Marrone, M. Antuono, A. Colagrossi, G. Colicchio, D. Le Touzé, and G. Graziani. δ-SPH model for simulating violent impact flows. *Computer Methods in Applied Mechanics and Engineering*, 200(13-16):1526–1542, 2011.
[19] S. Marrone, A. Colagrossi, D. Le Touzé, and G. Graziani. Fast free-surface detection and level-set function definition in SPH solvers. *Journal of Computational Physics*, 229(10):3652–3663, 2010.
[20] J. Michel. *Développements numériques de la méthode SPH couplée aux Eléments Finis appliqués au phénomène de l'hydroplanage*. PhD Thesis, Ecole Centrale de Nantes, July 2020.
[21] J. Michel, G. Oger, and D. Le Touzé. Effects of particle disordering on local and global fluid volume in the SPH method and proposition of an improved SPH-ALE scheme. In *Proceedings of the* 13^{th} *international SPHERIC workshop*, pages 275–282, 2018.
[22] J.J. Monaghan. On the problem of penetration in particle methods. *Journal of Computational Physics*, 82:1–15, 1989.
[23] J.J. Monaghan. SPH without a Tensile Instability. *Journal of Computational Physics*, 159(2):290 – 311, 2000.
[24] J.J. Monaghan and R.A. Gingold. Shock Simulation by the particle method SPH. *Journal of Computational Physics*, 52(2):374–389, 1983.
[25] G. Oger, S. Marrone, D. Le Touzé, and M. De Leffe. SPH accuracy improvement through the combination of a quasi-Lagrangian shifting transport velocity and consistent ALE formalisms. *Journal of Computational Physics*, 313:76–98, 2016.
[26] A.N. Parshikov and S.A. Medin. Smoothed Particle Hydrodynamics using interparticle contact algorithms. *Journal of Computational Physics*, 180:358–382, 2002.
[27] N.J. Quinlan, M. Lastiwka, and M. Basa. Truncation error in mesh-free particle methods. *International Journal for Numerical Methods in Engineering*, 66(13):2064–2085, 2006.
[28] P.W. Randles and L.D. Libersky. Smoothed Particle Hydrodynamics: some recent improvements and applications. *Computer methods in applied mechanics and engineering*, 39:375–408, 1996.
[29] G.A. Renaut. *Schémas d'ordre élevé pour la méthode SPH-ALE appliquée à des simulations sur machines hydrauliques*. PhD thesis, Ecole Centrale de Lyon, December 2015.
[30] P L Roe. Characteristic-Based Schemes for the Euler Equations. *Annual Review of Fluid Mechanics*, 18(1):337–365, 1986.
[31] A. Skillen, S. Lind, P.K. Stansby, and B.D. Rogers. Incompressible smoothed particle hydrodynamics (SPH) with reduced temporal noise and generalised fickian smoothing applied to body–water slam and efficient wave–body interaction. *Computer Methods in Applied Mechanics and Engineering*, 265:163 – 173, 2013.
[32] P.N. Sun, A. Colagrossi, S. Marrone, M. Antuono, and A.-M. Zhang. A consistent approach to particle shifting in the δ-plus-SPH model. *Computer Methods in Applied Mechanics and Engineering*, 348:912 – 934, 2019.

[33] P.N. Sun, A. Colagrossi, S. Marrone, and A.M. Zhang. The δplus-SPH model: Simple procedures for a further improvement of the SPH scheme. *Computer Methods in Applied Mechanics and Engineering*, 315:25 – 49, 2017.
[34] P.N. Sun, A.-M. Zhang, S. Marrone, and F. Ming. An accurate and efficient SPH modeling of the water entry of circular cylinders. *Applied Ocean Research*, 72:60 – 75, 2018.
[35] G. Taylor and A.E. Green. Mechanism of the production of small eddies from large ones. *Proceedings of the Royal Society of London Series A*, 158:499–521, 1937.
[36] B. Van Leer. Towards the ultimate conservative difference scheme. v. a second-order sequel to godunov's method. *Journal of Computational Physics*, 32(1):101 – 136, 1979.
[37] J.-P. Vila. On particle weighted methods and Smooth Particle Hydrodynamics. *Mathematical Models & Methods in Applied Sciences*, 9(2):161–209, 1999.
[38] H. Wendland. Piecewise polynomial, positive definite and compactly supported radial functions of minimal degree. *Advances in Computational Mathematics*, 4(4):389–396, 1995.
[39] R. Xu, P. Stansby, and D. Laurence. Accuracy and stability in incompressible SPH (ISPH) based on the projection method and a new approach. *Journal of Computational Physics*, 228(18):6703–6725, 2009.